

The CFHT Open Star Cluster Survey II – Deep CCD Photometry of the Old Open Star Cluster NGC 6819

Jasonjot Singh Kalirai¹

*Physics & Astronomy Department, 6224 Agricultural Road, University of British Columbia,
Vancouver, BC V6T-1Z1*

`jkalirai@physics.ubc.ca`

Harvey B. Richer¹

Gregory G. Fahlman^{1,2}

Jean-Charles Cuillandre²

Paolo Ventura³

Francesca D’Antona³

Emmanuel Bertin⁴

Gianni Marconi⁵

and

Patrick R. Durrell⁶

ABSTRACT

We present analysis of deep CCD photometry for the very rich, old open star cluster NGC 6819. The science goals are to catalogue the white dwarfs in the cluster and measure the cluster luminosity and mass functions. These CFH12K data results represent the first of nineteen open star clusters which were imaged as a part of the CFHT Open Star Cluster Survey. We find a tight, very rich, main-sequence and turn-off consisting of over 2900 cluster stars in the V, B–V color-magnitude diagram (CMD). Main-sequence

¹University of British Columbia

²Canada-France-Hawaii Telescope Corporation

³Osservatorio Astronomico di Roma

⁴Institut D’Astrophysique De Paris

⁵European Southern Observatory

⁶Penn. State University

fitting of the un-evolved cluster stars with the Hyades star cluster yields a distance modulus of $(m-M)_V = 12.30 \pm 0.12$, for a reddening of $E(B-V) = 0.10$. These values are consistent with a newly calculated theoretical stellar isochrone of age 2.5 Gyrs, which we take to be the age of the cluster. Both the depth gained in the photometry and the increased projected area of the CFH12K Mosaic CCD allow for detailed star counts in concentric annuli out to large angular radii. These indicate a much larger cluster extent ($R = 9'.5 \pm 1'.0$), by a factor of ~ 2 over some previous estimates. Incompleteness tests confirm a slightly negatively sloped luminosity function extending to faint ($V \sim 23$) magnitudes which is indicative of a dynamically evolved cluster. Further luminosity function and mass segregation tests indicate that low mass objects ($M \leq 0.65M_\odot$) predominate in the outer regions of the cluster, $3'.5 \leq R \leq 9'.5$. The estimation of the number of white dwarfs in NGC 6819, based on stellar evolution models, white dwarf cooling timescales, and conservation of star number arguments applied to the red giant stars of the cluster are in good agreement with the observed number. For those white dwarf candidates which pass both a statistical subtraction that removes background galaxies and field stars, and a high star/galaxy confidence by using image classification, we show comparisons to white dwarf isochrones and cooling models which suggest the need for spectroscopy to confirm the white dwarf nature of the brighter objects. This is entirely feasible for all objects, before a statistical subtraction cut, with the current generation of 8 meter class telescopes and multi-object spectrometers.

Subject headings: color-magnitude diagrams – open clusters and associations: individual (NGC 6819) – stars: luminosity function, mass function – white dwarfs

1. Introduction

The primary goal of the CFHT Open Star Cluster Survey is to catalogue a large number of white dwarf stars and provide observational constraints to the theoretical models of intermediate and young stellar clusters and their inhabitants (see §1 of Kalirai et al. 2001a, hereafter Paper I). These models, such as those for the initial-final mass relationship of the progenitor white dwarf star, or the upper mass limit to white dwarf production, have never been tested with the detail that is now possible. Studies involving white dwarf stars in open clusters have been limited for four major reasons: (1) the majority of these clusters are not old enough to have produced a sizeable white dwarf population, (2) most are not rich enough to contain numerous white dwarfs, (3) these clusters lie in the plane of the Galaxy so that foreground and background contamination is high, and (4) the photometric depth of most previous studies is not deep enough to clearly see white dwarfs. The first two factors result in very few white dwarfs, often quite scattered somewhere in the faint, blue end of the CMD, and the third results in a large amount of contamination from both field stars and background galaxies, which also appear as faint, blue objects. The fourth factor has

always been a deterrent to the serious study of cluster white dwarfs. White dwarf cooling models (Wood 1994; Bergeron 1995), indicate that a significant number of white dwarfs are not expected brighter than an absolute magnitude of $M_V \sim 10$. At the opposite end, it is known that very old, cool white dwarfs may reach $M_V \sim 17.5$. Even the bright end of the white dwarf cooling sequence is often too faint for the limiting magnitude that could possibly be reached by many telescopes, even for moderately close clusters. The new large field detectors and imagers on 4 m class telescopes are ideal instruments to study these faint magnitudes in open star clusters. This was demonstrated in the white dwarf analysis of M67 (Richer et al. 1998). The current data set for NGC 6819 is ideal for white dwarf studies because the cluster is both old and rich, and the photometry extends to faint, $V \sim 25$ magnitude, stars.

NGC 6819 was identified as an old stellar system almost 30 years ago (Lindoff 1972; Auner 1974). These early studies used photographic plates or photoelectric detectors and concentrated on bright stars. Cluster ages were determined by calibrating relative positions of turn-off and red giant branch stars on the CMD and by comparing the bright stars in the cluster to those of the evolved system M67. These methods produced a large range of ages for the cluster: 2 Gyrs (Lindoff 1972) – 4 Gyrs (Kaluzny & Shara 1988). More recently, a detailed isochrone fit to the cluster photometry has been carried out by Rosvick and VandenBerg (1998), and a new age estimate of 2.4 Gyrs has been determined using models with a significant amount of convective core overshooting (the age dependent on the amount of overshooting). The limiting magnitude of their CCD photometry ($V \sim 18.5$), the deepest for this cluster at the time, is too bright to include the low mass main-sequence stars and far too bright to detect any cluster white dwarfs.

Isochrone fitting has been commonly used to constrain the age measurement for star clusters. The difficulty is often in determining key parameters for the cluster such as the reddening, distance modulus, and metallicity. The uncertainty in these values can lead to an ambiguous isochrone fit. For NGC 6819, the reddening value causes the largest concern as $E(B-V)$ has ranged in the literature from 0.30 (Lindoff 1972; Auner 1974), to $E(B-V) = 0.12$ (Burkhead 1971). The earlier high estimates have been acknowledged as being derived from poor U filter photographic photometry. More recently, a reddening value of 0.15 (Canterna et. al. 1996) from photoelectric observations was found to agree with that obtained by Burkhead (1971). The latest value is given as $E(B-V) = 0.16$ for the reddening, and $(m-M)_V = 12.35$ for the distance modulus (Rosvick & VandenBerg 1998). This reddening value has been determined by first comparing the red giant clump of NGC 6819 with that of M67, and then adjusting the value slightly based on the theoretical isochrone fits. Additionally, a recent spectroscopic study of the red clump stars in NGC 6819 has yielded a reddening value of $E(B-V) = 0.14 \pm 0.04$ (Bragaglia et al. 2001), for a cluster metallicity of $[Fe/H] = +0.09 \pm 0.03$.

In the next section we briefly discuss the observations that have been obtained for this study. This is followed by a short discussion of the reduction procedures (a more complete discussion is given in Paper I). The science goals are then addressed one at a time by first determining the center and radial extent of the cluster which is a key for accurate star counts. We then discuss

star/galaxy classification, present our CMD and derive the distance to the cluster. This distance and the reddening are used to fit a new generation of isochrones (calculated especially for this project) and determine the cluster age. Next we present luminosity functions, mass functions, and binary star analysis for NGC 6819 which provide insight into the dynamical evolution of the cluster. Finally, we provide a detailed analysis of the white dwarf candidates in NGC 6819 which raise further questions and motivate spectroscopic classification.

2. Observations and Reductions

The observational data for NGC 6819 comes from the first night of a three night observing run in October 1999, using the CFH12K mosaic CCD on the Canada-France-Hawaii Telescope. This CCD contains 12 2048×4096 pixel ($0''.206$) chips that project to an area of $42' \times 28'$ on the sky, which is much larger than the cluster's radius, $\sim 9'.5$. We obtained nine 300 second images in both B and V, as well as single 50 and 10 second images in each filter. At a later time, we also acquired short 1 second frames so as to obtain unsaturated images of the bright stars in the cluster. Blank field images are not necessary as the outer four chips of the mosaic can be used to correct for field star and galaxy contamination. The seeing for the images deviated slightly from mean values of $0''.70$ in V and $0''.90$ in B (see Table 1). Photometric skies combined with this good seeing produced very sharp images of the cluster. A true color image created from the processed V, B and R images is shown in Figure 1.

We also obtain several flat-field, bias, and dark frames in order to pre-process the data. We chose to process the data using the FITS Large Images Processing Software (FLIPS), which was developed by Jean-Charles Cuillandre at CFHT (Cuillandre 2001). FLIPS is a highly automated package which performs similar tasks to the IRAF option **mscred**. A more detailed discussion of the processing using FLIPS can be found in §3.1.1 of Paper I. Additionally, the methods employed within FLIPS to average the nine images in V and B are discussed in §3.1.2 of the same paper. These individual images were dithered from one another to prevent stars from landing on bad pixels in more than one image.

The photometric calibration was obtained from numerous exposures of the Landolt standard field SA-92 (Landolt 1992). Detailed methods used to calibrate the data set are discussed in §§5.1 and 5.2 of Paper I. Table 2 of Paper I summarizes the number of exposures that were obtained in each filter and exposure time for SA-92, and Table 3 summarizes the number of stars (of varying air-mass) that were used on each CCD to calibrate the data. The photometric uncertainty in the zero points for the standard stars during this night was measured to be ~ 0.015 in V and ~ 0.014 in B. The air-mass coefficients were determined to be 0.088 ± 0.01 in V and 0.165 ± 0.005 in B, both in good agreement with CFHT estimations of 0.10 and 0.17 respectively. The color terms were averaged over the three night observing run and are in agreement with CFHT estimations in the V filter and slightly lower than estimations for the B filter.

The data was reduced using a preliminary version of the new TERAPIX photometry routine PSFex (Point Spread Function Extractor) (E. Bertin 2000, private communication). This program is a new part of SExtractor (Bertin & Arnouts 1996), which is commonly used for star/galaxy classification. We use a separate, variable PSF for each CCD in the mosaic. Further information on PSFex can be found in §4 of Paper I.

3. Star Counts and Cluster Extent

The existing measures of the apparent diameter of NGC 6819 makes it one of the smallest, rich open star clusters known. No clear definition of the methods used to determine the previously adopted cluster size have been published, however these results were derived using much smaller CCDs or photographic/photoelectric instruments which do not include a significant estimation of the background stars directly around the cluster. Most early estimates favored a larger cluster radius of 7' (Barkhatova, 1963) or 6.5' (King, 1964; Burkhead, 1971), although some are as small as 4' (Lindoff, 1972). Each of the CFH12K CCDs are 7' in their shortest direction, and therefore the entire cluster would be concentrated within the inner 4 of the 12 CCDs if we center the cluster in the middle of the mosaic. To determine the cluster center we first count stars in thin vertical and horizontal strips across the mosaic. This method is valid since there is no obvious trend in the background distribution, therefore suggesting no biases from differential extinction across the CCD's. The resulting profile was less than gaussian in shape, and produced limitations on the accuracy with which the center could be determined. An alternative approach which we implemented consisted of estimating the center, and then counting the number of stars in four equal quadrants around this center. Next we moved the center location around a small area and re-counted the number of stars until the value agreed in all four quadrants. Both approaches lead to similar values which estimate the center of the cluster to be at (x,y) = (6250,4020) on a global coordinate system ($\alpha_{J2000} = 19^h 41^m 17.7^s$, $\delta_{J2000} = +40^\circ 11' 17''$). The error in each of the x and y directions is ~ 40 pixels ($8''.2$). This system combines the 6 chips (horizontal) and 2 chips (vertical) on the mosaic (2048 pixels horizontal/CCD \Rightarrow 12288 total and 4096 pixels vertical/CCD \Rightarrow 8192 total) into one coordinate system taking into account the gaps between the CCDs. This estimate places the center of the cluster in the top right hand corner of chip 02 (see Figure 2).

The extent of NGC 6819 can now be found by counting the number of stars in different annuli around the center of the cluster (see Figure 2). To avoid significant biases from selection and incompleteness effects, we only use the stars with $15 \leq V \leq 20$. Each successive annulus that we use is 1' in width, with the exception of those near the center of the cluster (see Table 2 for annulus geometry). The value of the number of stars in each annulus is then normalized by the area of the respective annulus. We expect a drop off and stabilization in the resulting distribution of number of stars vs. radius from the center as soon as we clear the cluster and are simply counting the constant background. This approach is the first ever for this cluster and is only made possible due to the large size of CFH12K. Figure 3 shows the results for the extent of NGC 6819, and indicates

the cluster to be larger than all previous estimates. We find a drop off caused by the boundary of the cluster and the background between $R = 8'0-9'5$ ($1' = 290$ pixels). There are most likely still a very small number of cluster member stars outside of $R = 9'5$, however it is difficult to resolve these from background.

3.1. Comparison to King Model

The mass range of the stars on the main-sequence between the two magnitude cuts given above is not very large ($0.70 - 1.5 M_{\odot}$). In a classic series of papers King (1962; 1966) described how the density distributions of stars in globular clusters, open clusters, and some elliptical galaxies can all be represented by the same empirical law. This single-mass density law is very simple to use and involves only three parameters: a numerical factor, a core radius, and a limiting (tidal) radius. For systems with a large range in mass (more than a factor of 10), there are also more complicated multi-mass King models that can be used to represent density profiles with more relaxed constraints on mass ratios and distributions (eg. DaCosta & Freeman 1976). In order to fit a King model to the density profile shown in Figure 3, we first subtract off the background star counts from each annulus (described in §6.1). Next we determine a value for the tidal radius of NGC 6819. The tidal radius of a star cluster could potentially cause the cluster extent to be truncated at a finite value. This is determined by the tidal influence of massive objects in the Milky Way (eg. GMCs), which will remove the highest velocity stars from the cluster as they venture out to large distances from the center. The tidal radius for NGC 6819 can be estimated using equation (1),

$$r_t \sim \left(\frac{m}{3M}\right)^{1/3} D, \quad (1)$$

where m is the mass of the cluster ($\sim 2600M_{\odot}$) (see §7), M is the mass of the Galaxy within the cluster orbit, and D is the Galactocentric distance (Clemens 1985) of NGC 6819 (8.17 kpc). Therefore, the tidal radius for NGC 6819 is $r_t \sim 17$ pc, much larger than the cluster radius (~ 6.9 pc). Additionally, Wielen (1991) showed that it is not expected that a cluster of the size and mass of NGC 6819 would be dissolved before a minimum age of ~ 7 Gyrs (much older than the cluster age). This analysis takes into account both the effects of the Galactic tidal field for internal and external processes of cluster dissolution, and the evaporation of a star cluster due to its internal relaxation (see §6.2). With an estimate of the tidal radius of NGC 6819, we then fit a simple King model to the data and adjust the value of r_c until the best fit is obtained. r_c is strictly a model parameter in a King profile and has no physical meaning, although for many clusters it corresponds to the radius at which the surface brightness drops to half the central value. The best fit obtained is at $r_c = 1.75$ pc, and this profile is shown in Figure 4 to agree very well with the data.

4. Stellarity

Source classification is very important for studies of faint objects in the cluster so that an accurate distinction between star or galaxy can be made. The star/galaxy cut will affect both evolutionary tests of stars that become white dwarfs and the luminosity function for these stars. Our data set extends to $V \sim 25$ implying that most of the objects measured here are faint and have low signal to noise ratios. We use SExtractor (Bertin & Arnouts 1996) to assign a stellerity index to all objects on all CCDs in our data. This stellerity index is determined through a robust procedure that uses a neural network approach. The coefficients of this neural network were found by Emmanuel Bertin by training the routine in simulations of artificial data. The classification scheme attempts to determine the best hypersurface for an object which can be described by either of two different sets of parameter vectors; one for stars and the other for galaxies.

Figure 5 shows the variation of this stellerity index with magnitude. The difficulty arises in choosing a confidence limit to separate out stars from galaxies. Objects with an index of 0 are most likely galaxies and objects with an index of 1 appear stellar. Previous studies not involving faint objects have often adopted a very high, 0.95, cutoff (eg. von Hippel and Sarajedini 1998). However, some of the objects in the ‘clump’ seen in Figure 5 at $23 \leq B \leq 24.5$ and $0.75 \leq \text{stellerity} \leq 0.95$ are most likely stars. We find a clear separation between a white dwarf cooling sequence and background objects at approximately a 0.50 stellerity limit, and an even better separation at 0.75, however at this more strict cut we lose some faint objects (see §9.2). Later, we will use a statistical method to eliminate possible galaxies and background objects. We note however that it is difficult to determine this cut accurately without a spectroscopic classification for these objects.

We can estimate the number of galaxies that we expect in our cluster field (inner 9'5), by considering galaxy counts (Woods & Fahlman 1997) at high latitude and correcting for extinction in our field. Based on these statistics and prior to any stellerity cut, there are far more objects in our faint magnitude bins than the number of expected galaxies. For example, we expect less than 7% of all objects to be galaxies for $21 \leq V \leq 22$, less than 22% for $22 \leq V \leq 23$, whereas the number of expected galaxies rises to $\sim 70\%$ for $23 \leq V \leq 24$. Clearly, this last bin is of interest as the number of expected galaxies is comparable to the total number of all objects. However, after applying a 0.75 stellerity cut, we eliminate 1673 of 1701 objects from this bin, a number far greater than the number of expected galaxies, 1189. Therefore we can conclude that a significant number of faint objects in the cluster field are most likely stellar, however we may need to relax our 0.75 stellerity cut to include some of these fainter stars. A cut at 0.50 provides a better agreement between the number of objects thrown out and the number of expected galaxies. Further details of the stellerity index of faint blue objects in NGC 6819 is given in §9.

5. The NGC 6819 Color-Magnitude Diagram

Figure 6 exhibits CMDs for both the entire cluster ($R \leq 9.5$) and a blank field taken from an equal area of the outer chips on the mosaic. The cluster CMD (left) shows a very tight main-sequence and turn-off region. For this diagram we adopt a 0.50 stellarity confidence limit. The short 1 second exposures have allowed for the measurement of a red giant clump and a giant branch at the bright red end of the CMD. A significant contribution of these red giant stars is rare in most open clusters due to their young age and poor population, but are crucial for testing stellar models (see §5.2). Some potential white dwarf candidates can also be seen in the faint blue end of the CMD. Further analysis of these stars is presented in §9 where we fit cooling curves to the white dwarf sequence after eliminating field objects and applying more stringent confidence limits. We also note the presence of a significant contribution from approximately equal mass binary stars in the cluster. This sequence, which lies slightly above and parallel to the main-sequence, is discussed in §8.

5.1. Cluster Distance by Main-Sequence Fitting

NGC 6819 is four times the age of the Hyades (Perryman et al. 1998) and therefore a much smaller region of the CMD is available to fit to the Hyades main-sequence fiducial for the cluster distance because the high mass stars have evolved off the main-sequence. Fortunately, our deep CCD photometry provides a longer un-evolved main-sequence for the fitting. Distance determination by main-sequence fitting is also highly dependent on the adopted reddening value of the cluster. For a reddening of $E(B-V) = 0.10$, we find $(m-M)_V = 12.30 \pm 0.12$. Correcting for extinction ($A_V = 3.1E(B-V)$), the absolute distance to NGC 6819 is therefore 2500 pc. Our value is slightly larger than most previous studies due to the lower adopted reddening value: Rosvick and VandenBerg (1998) ($d = 2350$ pc), Auner (1973) ($d = 2170$ pc), and Lindoff (1972) ($d = 2200$ pc).

5.2. Theoretical Isochrones

Testing theoretical stellar evolutionary models requires knowledge of the cluster metallicity, reddening, and distance. This testing is very important in order to further refine the models. For example, theoretical models involving the amount of convective core overshooting that should be used or the temperature at which the slope changes at the faint end occur (caused by opacity effects), lack observational constraints. Additionally, the testing allows for an age determination for the cluster. The present photometry of NGC 6819 is ideal for these comparisons as there are a large number of stars on a tightly constrained main-sequence. The turn-off of the cluster, as well as the red giants and giant branch stars are also useful as they allow for tests of stars in the helium burning phases of evolution. These are important for model calibration.

The tracks were built by adopting the ATON2.0 code for stellar evolution, a detailed description of which can be found in Ventura et al. (1998). Convection has been addressed within the Full Spectrum of Turbulence (FST) framework (Canuto & Mazzitelli 1992). Chemical mixing and nuclear burning have been treated simultaneously with a diffusive scheme: convective velocities have been computed according to eqs. (88), (89) and (90) in Canuto et al. (1996). Core-overshooting in the models has been described by means of an exponential decay of turbulent velocity out of the formal convective borders as fixed by Schwarzschild’s criterion; this behavior of velocity is consistent with approximate solutions of the Navier-Stokes equations (Xiong 1985), and with the results of numerical simulations (Freytag et al. 1996). A value of $\zeta = 0.03$ of the free parameter giving the e-folding distance of the exponential decay has been adopted. We adopt grey atmospheres for all models of mass above $0.6 M_{\odot}$. For masses $M \leq 0.6 M_{\odot}$ the models of Montalbán (2001), which adopt boundary conditions derived from the non grey model atmosphere grid NextGen (Hauschildt, Allard & Baron 1999), are employed. The isochrone has been calculated by interpolating in mass between the stellar tracks, according to the scheme by Pols et al. (1998). Finally, the transformations between the theoretical and the observational plane have been accomplished by adopting the colors of Bessel et al. (1998).

Figure 7 shows the fit of the NGC 6819 data to a 2.5 Gyr old stellar isochrone. We use a reddening value of $E(B-V) = 0.10$ and a derived distance modulus of $(m-M)_V = 12.30 \pm 0.12$ for this and further theoretical comparisons. It is clearly seen that the slope of the bright main-sequence as well as the turn-off and red giant clump are all in excellent agreement with this model, which uses $Z = 0.02$. Although still quite good, the fit to the lower main-sequence is slightly blue of the data, which could be a result of the photometric calibration of the data or, alternatively, the color transformations in the model.

6. Luminosity Functions

The CMD of NGC 6819 indicates some similarities to other old open star clusters such as M67, NGC 6633, NGC 752 (Francis 1989), and NGC 188 (von Hippel & Sarajedini 1998) with regards to the distribution of stars. For example, by simply looking at the density of stars along the main-sequence as a function of magnitude, it is clear that the majority of the cluster members are bright, not faint. After accounting for incompleteness at the faint end, such an effect can be investigated by accurately counting the number of cluster stars as a function of magnitude. This resulting luminosity function for such a cluster will clearly be either flat ($\frac{dN}{dM_V} \sim 0$) or slightly negatively sloped ($\frac{dN}{dM_V} \leq 0$). We define the cluster stars by first creating a main-sequence fiducial (clipping the color at 3.5σ from the mean) after isolating the main-sequence from the background distribution. We then use a clipping routine to create an envelope around this fiducial based on the errors of the stars (envelope broadens out towards faint magnitudes). The counting of the stars is done within this envelope, for both the cluster CMD and the background CMD (Figure 6), with the cluster luminosity function coming from the difference between the counts in the two fields.

However, in order to accurately count stars, we must first determine incompleteness corrections.

6.1. Incompleteness Corrections

The combination of cluster, telescope, detector, and reduction routines leads to an incompleteness factor in the number of detected objects. For bright stars, this factor is typically negligible, however, for fainter stars ($V \geq 20$) it becomes increasingly more important to determine how many stars have been missed in the study. In order to better understand the incompleteness of our data we produce an artificial catalogue of input stars for which we know the magnitudes and colors. We add a small number of stars uniformly in 5 trials so as not to affect the crowding statistics of the field, and eventually obtain a distribution of stars that lie on a similar slope to the raw luminosity function of the cluster. Next, we reduce this data set in an identical manner to the data in the cluster and measure the number of stars per magnitude bin that were recovered (see Figure 8). An identical analysis is also carried out for the background fields. The completeness corrected number of stars in the cluster can then be determined in 3 steps. First, we multiply the cluster field incompleteness correction by the number of stars in the cluster. Second, we multiply the blank field incompleteness correction by the blank field stars. Finally, we subtract the two and obtain the corrected star counts. In this analysis the cluster field stars are simply the stars for the respective annuli in the inner $9'5$ of the center of the cluster. For the blank field star counts, we use all of the stars in CCDs 00, 06 and 11 (ie. three of the outer four in Figure 2) as well as the outer parts of the intermediate CCDs (01, 04, 07 and 10), and then scale the numbers to match the area of the corresponding inner cluster annuli. This approach works well as we have shown that the cluster extent ($9'5$) does not extend half way into the intermediate CCDs (01, 04, 07 and 10) (see Figure 3). CCD 05 is ignored in the background as it has a very low sky background level and we found some abnormal zero point shifts and other errors throughout the analysis.

As expected we find that the current data set is quite complete at the bright to intermediate magnitudes, however it becomes increasingly more incomplete towards the faint end (60% complete at $V \sim 22$). Incompleteness variations due to annuli are very small as the crowding is not a significant concern for these fields. However, we note that the incompleteness corrections were slightly higher for faint magnitudes in chip 02, which is also the CCD in which the center of the cluster resides. This is most likely due to crowding and scattered light from the slight over-density of bright stars. The incompleteness corrections for bright stars are almost identical for the inner vs outer annuli.

For the white dwarf sequence in NGC 6819, we determine an incompleteness correction based on a set of artificial stars distributed at this location in the CMD ($21 \leq V \leq 25$, $-0.25 \leq B-V \leq 0.4$). Here, we choose a constant function, which produces an equal number of objects per magnitude bin (see Figure 8). This is a good method for the white dwarfs in the cluster as our data set is not faint enough to detect the end of the cooling sequence so there is negligible piling-up of stars at faint magnitudes. As expected, the incompleteness corrections for these stars are less (they are more

complete) than for the main-sequence stars at a given magnitude because they are brighter in the B band for a given V magnitude. These results are important for continuity arguments presented in §9.1. Incompleteness findings for both the main-sequence and the white dwarf sequence are summarized in Table 3.

6.1.1. Incompleteness Errors

With these star counts, it is also important to have an estimation of the errors. Bolte (1989) gives a careful account in determining incompleteness errors in the analysis of M30. This reasoning assumes that the counting uncertainties are derived from a Poisson distribution, and that the artificial star count uncertainties are derived from a binomial distribution. Furthermore the errors in the incompleteness and the raw star counts are assumed to be uncorrelated. If we write the corrected number of stars in any magnitude bin as $n = \frac{n_{obs}}{f}$, where n_{obs} is the raw counts in the bin, and f is the ratio of the number of recovered artificial stars to the number added for each magnitude bin ($f = \frac{n_{recovered}}{n_{added}}$), then the variance in n is

$$\sigma_n^2 = \sigma_{n_{obs}}^2 \left(\frac{\partial n}{\partial n_{obs}}\right)^2 + \sigma_f^2 \left(\frac{\partial n}{\partial f}\right)^2. \quad (2)$$

The variance in n_{obs} is simply $\sigma_{n_{obs}}^2 = n_{obs}$, and the variance in f is $\sigma_f^2 = \frac{f(1-f)}{n_{added}}$. Performing the partial differentiations in equation (2) gives the desired variance in n ,

$$\sigma_n^2 = \frac{n_{obs}}{f^2} + \frac{(1-f)n_{obs}^2}{n_{added}f^3}. \quad (3)$$

We use this method of determining errors for both the field and background stars, and then add the errors for the difference in quadrature.

The final corrected star counts are presented in Table 4. In this table, the first row of each magnitude bin consists of raw counts (cluster field – blank field) whereas the row underneath this one contains the incompleteness corrected numbers (correction applied from Table 3). Also shown in parentheses are the errors in these counts, as calculated from the analysis given above. The corresponding global luminosity function is plotted in Figure 9, where the dashed line represents the raw counts and the solid line the incompleteness corrected counts. As expected, the luminosity function is almost flat (slightly negatively sloped), most likely due to dynamical evolution in this relaxed cluster (see §6.2). We do not see a drop off at the faint end of the luminosity function. Although large errors make it difficult to determine, this evidence suggests that the lowest mass main-sequence stars may not have been detected in this deep photometry. Integrating the luminosity function and accounting for the evolved stars brighter than $V = 15$, gives a lower limit to

the total cluster population of ~ 2900 stars. This number makes NGC 6819 one of the richest open star clusters known.

6.2. Dynamical Relaxation

The cluster luminosity function is determined by the initial mass function as well as the subsequent effects of dynamical evolution to the present epoch. The initial distribution of stars *of any mass* will roughly follow a density profile given by a King model – ie. an isothermal sphere (Binney & Tremaine 1987). Therefore the initial density of stars for any mass will always be highest in the center of the cluster and decrease as a function of increasing radii from the center. Equipartition of energy between the stars of different masses occurs on a timescale characterized by the relaxation time of the cluster. If the cluster is older than its relaxation time, then we can expect that the stellar encounters within the cluster have caused the stars to relax rapidly toward equipartition, with low mass stars travelling faster than the high mass stars. To estimate the relaxation time for NGC 6819, we must first determine the crossing time of a star across the cluster, $t_{cross} = \frac{R}{v}$. Since we know both the distance to the cluster (see §5.1) and its angular extent (see §3), it is trivial to solve for the linear radius (~ 6.9 pc). Additionally, the velocity of a star across the cluster can be calculated using $v^2 \sim \frac{GNm}{R}$, where Nm is the mass of the cluster (estimated in §7). The relaxation time is then given by equation (4),

$$t_{relax} \sim t_{cross} \frac{N}{8 \ln N}, \quad (4)$$

where $\frac{N}{8 \ln N}$ is the number of crossings of a star which are required for its velocity to change by an order of itself (Binney & Tremaine 1987). NGC 6819 is a very rich cluster, with about 2900 stars (see §6.1.1), which gives a relatively large relaxation time compared to average open clusters with several hundreds of stars. However, this relaxation time (220 Myrs) is still a factor of 10 smaller than the cluster age (2.5 Gyrs), so we expect the cluster to be relaxed: the lower mass stars gain energy through gravitational encounters with higher mass cluster stars (which sink to the center of the cluster) and slowly diffuse out of the cluster if their escape velocity is great enough (Hawley, Tourtellot & Reid 1999). Therefore, for NGC 6819, the lower mass stars are more likely to be observed at a larger radii than the high mass stars. The evolution does however depend on parameters such as binary fraction and cluster richness (de la Fuente Marcos 1997).

6.3. Mass Segregation

Mass segregation and evaporation of low mass stars have been suggested to occur in dynamically relaxed clusters since van den Bergh & Sher (1960) demonstrated from their photographic

data that many clusters had luminosity functions that apparently turned over at faint magnitudes, unlike that seen for the field stars. Subsequent observational studies suggested that the mass functions for some open clusters have changed over time due to dynamical evolution (Francic 1989; von Hippel & Sarajedini 1998; Raboud & Mermilliod 1998; Hawley, Tourtellot & Reid 1999). Some of these clusters are quite young, such as the Pleiades, but other such as NGC 2420 are as old as NGC 6819. There have also been some studies which show that intermediate aged clusters do not suffer from mass segregation. Sagar & Griffiths (1997) looked at mass segregation effects for five, distant open clusters and found that the effects are not correlated with cluster age. The major difference between the current study and these others, is that NGC 6819 is far richer in stellar content than most of these clusters and this affects the evolutionary scenario because the escape velocity increases with the cluster mass.

In order to look for evidence of mass segregation in NGC 6819, we produce three luminosity functions for different annuli from the center of the cluster. To keep the statistics reasonable we split the cluster into three components, a central portion (0'-2'5), middle portion (2'5-5'5), and outer portion (5'5-8'5). Figure 10 shows the luminosity function for each of these portions. We have normalized the luminosity function for each of the annuli with respect to the first annulus at $V = 17$. The shapes of the luminosity functions provide clear evidence for mass segregation in NGC 6819. The high mass stars on the main-sequence are clearly concentrated in the central regions of the cluster, whereas the outer annuli show a greater relative concentration of low mass stars.

In Figure 11 we plot six CMDs, each for an increasing radial annulus to show the richness of the main-sequence as a function of radial position. Clearly, the CMD for annulus A11 ($8'5 \leq R \leq 9'5$) contains very few main-sequence stars, which is consistent with Figure 3. The general trend from inner to outer annuli in this figure confirms that the faint stars are not centrally concentrated. Surprisingly, Figure 11 also shows a prominent binary sequence in the intermediate-outer regions of the cluster (see Annulus A6 $\rightarrow 3'5 \leq R \leq 4'5$). Binaries are discussed in §8.

7. Mass Functions

The mass function of a stellar population is typically expressed as the number of stars / unit mass / unit solid angle. Since it is the luminosity that is measured, not the mass, this mass function is usually expressed as in equation (5),

$$N(m) = N(M_V) \left[\frac{dM_V}{dm} \right]. \quad (5)$$

In this equation, m is the mass, $N(M_V)$ is the luminosity function, and $\frac{dM_V}{dm}$ is the mass-luminosity relation. Therefore, the observed luminosity function must be multiplied by the slope of the M_V -mass relation to obtain the mass function. Typically, the mass function is assumed to be a power law so that

$$\Psi(m) \propto m^{-(1+x)}, \quad (6)$$

where x takes on a value of 1.35 in the work of Salpeter (1955). A discussion of the observational constraints and differing values of this slope in young clusters, young field stars, old open clusters, low mass disk stars, globular clusters, and the Galactic spheroid and halo is given by Richer & Fahlman (1996). Additionally, Francic (1989) has shown that the mass functions for some old Galactic clusters (NGC 6633, NGC 752, and M67) are weighted towards the higher mass stars. This analysis also showed the slope of the mass function for younger open clusters to be about $x = 1$. The inverted mass function for the older clusters may be due to dynamical processes in the cluster which work to better retain the higher mass stars. We have shown that it is likely that these processes may have already occurred in NGC 6819 (see §6.2). In order to better quantify the dynamical evolution, we can observe the change in the mass function for different annuli from the center of the cluster.

We use the Rome theoretical isochrones (see §5.2) to create a mass-luminosity relationship for NGC 6819. The slope of this mass-luminosity relationship is used to convert the number of stars in each magnitude bin to the number of stars per unit mass. We derive the slope using the end points of each magnitude bin that is used in the analysis, and from this slope, derive the mass function. As expected, the global ($R \leq 9'5$) mass function (bottom-right of Figure 12) is almost flat ($\frac{dN}{dm} = \text{constant}$). Fitting a power law to this global function (as in equation (6)) gives a value of $x = -0.15$. For comparison, we also plot a Salpeter value ($x = 1.35$) in the global plot which is much steeper than the NGC 6819 mass function. Figure 12 also shows a series of mass functions for annuli at increasing radial distances from the cluster center. There is a systematic change in the slope of the mass function with increasing radius (positive slope \rightarrow negative slope) which is consistent with the expectations of dynamical evolution in NGC 6819. Integrating the global mass function provides a total cluster mass of $\sim 2600M_{\odot}$.

8. Binary Stars in NGC 6819

The early stages of the dynamical evolution of star clusters has been shown to be dominated by primordial binaries (Heggie & Aarseth 1992). These binaries can be explained by a number of different formation mechanisms: capture events, fragmentation processes during collapse of protostar, exchange events, and orbital decay (see de la Fuente Marcos 1996; Hartigan et al. 1994; Bodenheimer 1993). The presence of binaries in a cluster is expected to accelerate the cluster dispersion in the early stages of cluster evolution. Multicomponent cluster models indicate that the early evolution will be accelerated for sparse clusters and slowed down for very rich clusters (de la Fuente Marcos 1996). The effects of these binaries on the cluster environment are estimated to be less than the effects of stellar evolution. A study of the location of the binaries in NGC 6819 can be important for constraints on future models as well as comparisons to binary populations in younger clusters (Brandner et al. 1996; Ghez et al. 1993, 1994; Padgett et al. 1997).

In order to quantify the location of the equal mass binaries in NGC 6819, we create a fiducial that matches with the observed binary population in annulus A6, and isolate the sequence from the remaining stars on the CMD by eliminating objects that deviate by more than 3σ from the mean location of the fiducial. This annulus produced the most prominent binary sequence (observing by eye...see upper-right diagram in Figure 11), however it does not contain the highest fraction of binaries as the majority of the main-sequence stars are also concentrated here. The fiducial is located between $\Delta V = 0.72$ and 0.77 above the main-sequence fiducial depending on the magnitude. We then use this fiducial to count the number of stars in a thin strip centered on the fiducial in all annuli and the corresponding blank fields for each. The results after subtracting the cluster fields from the blanks are presented in Table 5. A lower limit for the global cluster equal mass binary content is found to be $\sim 11\%$, however the highest population is observed in the outer regions of the cluster (A9 = 18%, A10 = 25%). The errors in these values are large (parenthesis in Table 5) and it is difficult to speculate on any evolutionary effects of binaries from this data, however we do note that the equal mass binaries of NGC 6819 are more concentrated in the outer regions of the cluster (with the exception of A8). This is not expected as the binaries are higher mass and should sink to the center of a dynamically relaxed cluster. The reason for this may be that we are missing the most massive binaries in this analysis. The vertical $\Delta V = 0.76$ magnitude shift caused by a system with a mass-ratio of 1 (equal mass binaries) would cause the location of the massive objects to coincide with the turn-off of the main-sequence, therefore they are not counted in the present analysis.

9. White Dwarfs in NGC 6819

Studies involving old white dwarf stars in globular star clusters are very important for obtaining a lower limit to the age of the Universe. At present this can only be done with the Hubble Space Telescope as the end of the white dwarf cooling sequence for these clusters occurs at extremely faint magnitudes ($M_V = 17.5$ for age = 12 Gyrs (Richer et al. 2000)). Determining ages in this manner strongly depends on the theoretical models of cooling white dwarfs. It has been recently shown that old hydrogen rich white dwarfs may actually be much bluer than previously thought (Hansen 1999) due to atmospheric molecular hydrogen opacity effects. These new models predict a strong blue ‘hook’ in the CMD for the cooling white dwarfs at an age of ~ 8 Gyrs. Although the white dwarfs in NGC 6819 are far too hot to form molecular hydrogen which causes a suppression of flux in the infrared, they are important for calibration and confirmation of the validity of the models at brighter magnitudes that will be used in globular cluster studies.

9.1. Continuity Arguments and Field Object Subtraction

NGC 6819 is very rich in stellar content, thus a significant number of both hydrogen (DA) and helium (DB) white dwarfs are expected. We can predict the number of expected white dwarfs

above a limiting magnitude cut-off in the cluster by counting the number of stars in the red giant phase and applying a continuity argument for these stars. From the masses of the red giant stars and the Rome stellar evolutionary sequence, the lifetime of the red giants in the ‘clump’ ($V = 13$, $B-V = 1.2$) is determined to be 5×10^7 years for models with no convective overshooting and 9×10^7 years for an overshooting model. Clearly, we favour the latter model as it agrees better with our data. Additional evidence for the justification of core-overshooting models for NGC 6819 was given in detail in the analysis of Rosvick and VandenBerg (1998). The continuity argument which we apply to determine the number of expected white dwarfs (N_{WD}) follows from the hypothesis that all stars of mass less than $\sim 8 M_{\odot}$ will evolve in to white dwarfs. First we determine the number of objects in the red giant ‘clump’ (N_{RG}) after correcting for field star contamination; 13. Next we can use the white dwarf cooling models to determine the white dwarf cooling ages ($t_{cooling}$) at a certain magnitude ($V = 23, 23.5$, and 24) that the stars have cooled to, for varying white dwarf masses ($M = 0.5, 0.6$, and $0.7 M_{\odot}$). For post main-sequence evolution the number of stars in a given evolutionary phase is proportional to the time spent in that phase. Therefore, we can estimate the number of white dwarfs that we expect to see in the cluster and compare this with the number observed after both field star subtraction and incompleteness corrections (see §6.1), by using equation (7):

$$N_{WD}(\leq M_V) = \frac{N_{RG}}{t_{RGB}} t_{cooling}(\leq M_V). \quad (7)$$

The field star subtraction is addressed statistically by comparing the location of objects in the lower-left (faint-blue) section of the cluster CMD to the background field CMD. We take each object within this location on the background CMD and eliminate the corresponding closest object in the cluster CMD.

We can estimate the uncertainties in the expected number of white dwarfs in a similar manner to that used for the main-sequence stars: use Poisson errors for both the observed number of white dwarfs and red giants, and a binomial distribution for the incompleteness errors (see §6.1.1). Additionally, there is an uncertainty in the white dwarf cooling age which is found by multiplying the slope of the cooling curve by the error in the magnitude as determined by PSFex.

We find that for a model with a large amount of core-overshooting (this produces a larger convective core \rightarrow time in RG phase increases) the predicted number of white dwarfs far exceeds the number observed (to $V = 24$) at a strict 0.90 stellarity cut. However, the predicted number agrees very well if we impose a less stringent confidence limit of 0.80, especially for $0.7 M_{\odot}$ objects. Similar results are also seen for intermediate core-overshooting, where the number of predicted white dwarfs agrees well with the number observed up to $V = 23.5$. For a brighter magnitude cut of $V = 23$, we find too many white dwarfs in all but the low core-overshooting cases with $M = 0.6$ and $0.7 M_{\odot}$. It is difficult to make predictions from this analysis because the uncertainties remain large. The analysis however indicates that a core-overshooting model is preferred for the

cluster if we are to consider all potential white dwarfs to our limiting magnitude. This assumes that a substantial number fraction of the white dwarfs are not tied up in binaries. These results are summarized in detail in Table 6, with errors in parentheses.

9.2. White Dwarf Analysis

Figure 13 shows the CMD for the cluster before any source rejection (left) and after we have imposed some constraints (middle and right). The constraints are (1) only accept objects with a stellarity confidence index above 0.50 (middle), and (2) only accept those objects which also survive a statistical subtraction to remove field objects (right). Criterion (1) is arbitrary as explained in §4. Even at a 0.50 stellarity cut, some of these objects could still be faint unresolved galaxies, AGN, or some other non-cluster object. We note however, that a significant portion of the remaining objects are in fact stellar to within a 0.90 confidence. This is shown in more detail in Figure 14, where we have zoomed into the hot faint end of the CMD. Criterion (2) has been addressed by eliminating possible cluster field objects that are in the same vicinity of the CMD as background field objects as described in §9.1. We invoke this approach for a small region in the CMD surrounding and including all possible cluster white dwarfs (objects below the dashed line in Figure 13 (middle)). The statistical subtraction shows that there is an over-density of objects in the cluster field, however, we can not say for sure whether the objects that we have removed are in fact not cluster objects. In Figure 14 we also indicate the stellarity for each of the white dwarf candidates, which is found to be ≥ 0.90 for the majority of the objects above $V = 24$.

9.3. Interpretation of Cooling Sequence

The statistically subtracted and star/galaxy corrected CMD (Figure 13 (right)) indicates a clear separation between the white dwarfs and the field stars. This potential white dwarf cooling sequence is separated from these field stars by an average of ~ 0.6 magnitudes in color on the CMD. There are very few objects between the two populations. The putative white dwarf cooling sequence revealed however is not particularly tight as there is some evidence for a gap between this (the bluer objects) and an redder potential white dwarf sequence (apparent in Figure 14). For the adopted reddening value of the cluster, no reasonable mass white dwarf cooling sequence fits the reddest objects in this location of the CMD. It is unlikely that photometric spread is causing some of these objects (the redder objects) to deviate so much in color from those that agree with the $0.7 M_{\odot}$ cooling sequence (Wood 1994). To better judge this, we have plotted a photometric error bar as a function of magnitude at 0.5 magnitude intervals in Figure 14. These errors, as determined by PSFex, are consistent with those found for the recovered artificially added stars in the incompleteness tests. It is clear that the spread in data points is larger than the error bars. A more likely scenario to explain the positions of these objects in the CMD is that they are just excess background or foreground objects which were not removed in the statistical subtraction.

Alternatively, some could also be highly reddened background white dwarfs.

For those objects which closely follow the $0.7 M_{\odot}$ white dwarf cooling sequence we determine a luminosity function after correcting for both a 0.75 stellarity cut and an incompleteness correction. The slope of this luminosity function agrees very well with theoretical expectations (Fontaine 2001) (see Figure 15). The bright end of this theoretical function has been slightly extended to include our brightest objects. There is no obvious agreement with the theoretical function if all objects in Figure 14 are considered. Although we believe the bluest objects in this Figure to be bona-fide white dwarfs, spectroscopic confirmation is required for these as well as those that were eliminated in the statistical subtraction. Fortunately, multi-object spectroscopy with instruments such as GMOS on Gemini will allow measurement of multiple objects in the faint-blue end of the CMD.

10. Conclusion

We have obtained deep ($V \sim 25$) CCD photometry of a $42' \times 28'$ field centered on the old open star cluster, NGC 6819. This photometry indicates both a larger cluster extent ($\sim 9'.5$) and a much richer cluster population (~ 2900 stars, $2600 M_{\odot}$, after incompleteness corrections are applied) than previously estimated. Main-sequence fitting of the un-evolved stars in the cluster indicates a true distance modulus of $(m-M)_o = 11.99 \pm 0.18$ for a reddening value of $E(B-V) = 0.10$. Isochrone fits with up-to-date models are in excellent agreement with the data and comparison with turn-off stars in the cluster provides an age estimation of ~ 2.5 Gyrs. Measurements of the luminosity function and mass function of the cluster in concentric annuli indicate the cluster to be dynamically evolved. Studies of the cluster CMD suggest clear evidence for mass segregation in NGC 6819. A lower limit of 11% is found for the equal mass binary fraction in the cluster, although this number is up to a factor of two higher for some of the outer regions of the cluster. Analysis of the faint blue section of the CMD indicate ~ 21 high probability WD candidates brighter than $V = 23.5$. Most of these stars are scattered around a $0.7 M_{\odot}$ white dwarf cooling curve. Until we have spectroscopic confirmation of their WD nature, it is premature to determine the initial-final mass relationship for these stars.

REFERENCES

- Auner, G. 1974, *A&AS*, 13, 143
- Barkhatova, K.A., Dronova, V.I., Pareva, L.I. & Sjasjkina, L.P. 1963, *Collect. Works, Volume 1* (Ekaterinburg: Astron. Inst. Urals State Univ.), 3
- Bergeron, P. 1995, *PASP*, 107, 1047
- Bertin, E. & Arnouts, S. 1996, *A&AS*, 117, 393

- Bessel, M.S., Castelli, F. & Plez, B. 1998, *A&A*, 333, 231
- Binney, J. & Tremaine, S. 1987, *Galactic Dynamics* (Princeton: University Press)
- Bodenheimer, P., Ruzmaikina, T. & Mathieu, R.D. 1993, in: *Protostars and Planets III*, ed. E.H. Levy & J.I. Lunine (Tucson: Univ. Arizona Press), 367
- Bolte, M. 1989, *ApJ*, 341, 168
- Bradner, W., Alcalá, J.M., Kunkel, M., Moneti, A. & Zinnecker, H. 1996, *A&A*, 307, 121
- Bragaglia, A. et al. 2001, *AJ*, 121, 327
- Burkhead, M.S. 1971, *AJ*, 76, 251
- Canterna, R., Geisler, D., Harris, H., Olszewski, E. & Schommer, R. 1986, *AJ*, 92, 79
- Canuto, V.M.C. & Mazzitelli, I. 1992, *ApJ*, 389, 724
- Canuto, V.M.C., Goldman, I. & Mazzitelli, I. 1996, *ApJ*, 473, 550
- Clemens, D.P. 1985, *ApJ*, 295, 422
- Cuillandre, J-C. 2001, *A&A*, in preparation
- DaCosta, G.S. & Freeman, K.C. 1976, *ApJ*, 206, 128
- de la Fuente Marcos, R. 1997, *A&A*, 322, 764
- de la Fuente Marcos, R. 1996, *A&A*, 314, 453
- Fontaine, G. 2001, *PASP*, in press
- Francic, S.P. 1989, *AJ*, 98, 888
- Freytag, B., Ludwig, H.G. & Steffen, M. 1996, *A&A*, 313, 497
- Ghez, A.M., Emerson, J.P., Graham, J.R., Meixner, M. & Skinner, C. 1994, *ApJ*, 434, 707
- Ghez, A.M., Neugebauer, G. & Matthews, K. 1993, *AJ*, 106, 2005
- Hansen, B.M.S. 1999, *ApJ*, 520, 680
- Hartigan, P., Strom, K.M. & Strom, S.E. 1994, *ApJ*, 427, 961
- Hauschildt, P.H., Allard, F., & Baron, E. 1999, *ApJ*, 512, 377
- Hawley, S.L., Tourtellot, J.G., & Reid, I.N. 1999, *AJ*, 117, 1341
- Heggie, D.C. & Aarseth, S.J. 1992, *MNRAS*, 257, 513

- Kalirai, J.S., Richer, H.B., Fahlman, G.G., Cuillandre, J., Ventura, P., D'Antona, F., Bertin, E., Marconi, G. & Durrell, P. 2001a, *AJ*, 122, 257
- Kaluzny, J. & Shara, M. 1988, *AJ*, 95, 785
- King, I.R. 1962, *AJ*, 67, 471
- King, I.R. 1964, *Roy. Obs. Bull.* (No. 82), 106
- King, I.R. 1966, *AJ*, 71, 276
- Landolt, A. U. 1992, *ApJ*, 104, 340
- Lindoff, U. 1972, *A&AS*, 7, 497
- Montalban, J. 2001, in preparation
- Padgett, D.L., Strom, S.E. & Ghez, A. 1997, *ApJ*, 477, 705
- Perryman, M.A.C., Brown, A.G.A., Lebreton, Y., Gomez, A., Turon, C., de Strobel, G.C., Mermilliod, J.C., Robichon, N., Kovalevsky, J. & Crifo, F. 1998, *A&A*, 331, 81
- Pols, O.R., Schroder, K.P., Hurley, J.R., Tout, C.A. & Eggleton, P.P. 1998, *MNRAS*, 298, 525
- Raboud, D. & Mermilliod, J-C. 1998, *A&A*, 329, 101
- Richer, H.B. & Fahlman, G.G. 1996, *AIP Conf. Proc.* 393, 357
- Richer, H.B., Fahlman, G.G., Rosvick, J. & Ibata, R. 1998, *ApJ*, 504, L91
- Richer, H.B., Hansen, B., Limongi, M., Chieffi, A., Straniero, O. & Fahlman, G.G. 2000, *ApJ*, 529, 318
- Rosvick, J.M. & VandenBerg, D. 1998, *AJ*, 115, 1516
- Sagar, R. & Griffiths, W.K. 1998, *MNRAS*, 299, 777
- Salpeter, E.E. 1955, *ApJ*, 121, 161
- van den Bergh, S. & Sher, D. 1960, *Publ. David Dunlap Obs.*, 2, 203
- Ventura, P., Zeppieri, A., Mazzitelli, I. & D'Antona, F. 1998, *A&A*, 334, 953
- von Hippel, T. & Sarajedini, A. 1998, *AJ*, 116, 1789
- Wielen, R. 1991, in *ASP Conf. Ser. 13, The Formation and Evolution of Star Clusters*, ed. K. Janes (San Francisco:ASP), 343
- Wood, M.A. 1994, *AAS Meeting*, 185, 4601

Woods, D. & Fahlman, G. 1997, ApJ, 490, 11

Xiong, D.R. 1985, A&A, 150, 133

Fig. 1.— True-color image from the individual V, B and R 50 second frames. The image size is $42' \times 28'$.

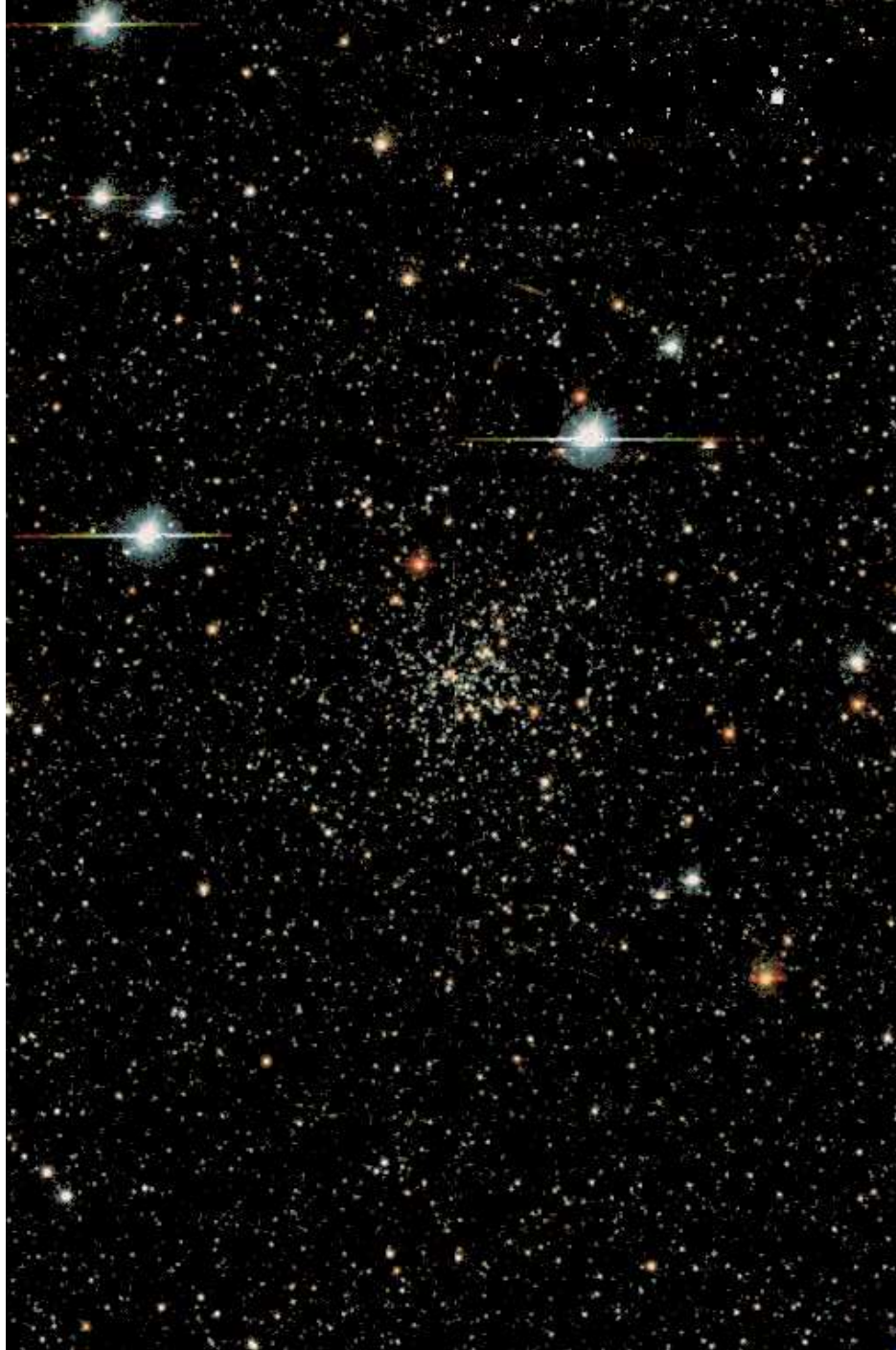


Fig. 2.— Orientation of the 12 chips of CFH12K are shown. The small x in chip 02 marks the approximate center of the cluster. The outer radii of four annuli separated by $2'$ ($1'5$, $3'5$, $5'5$, $7'5$ and $9'5$) are also shown.

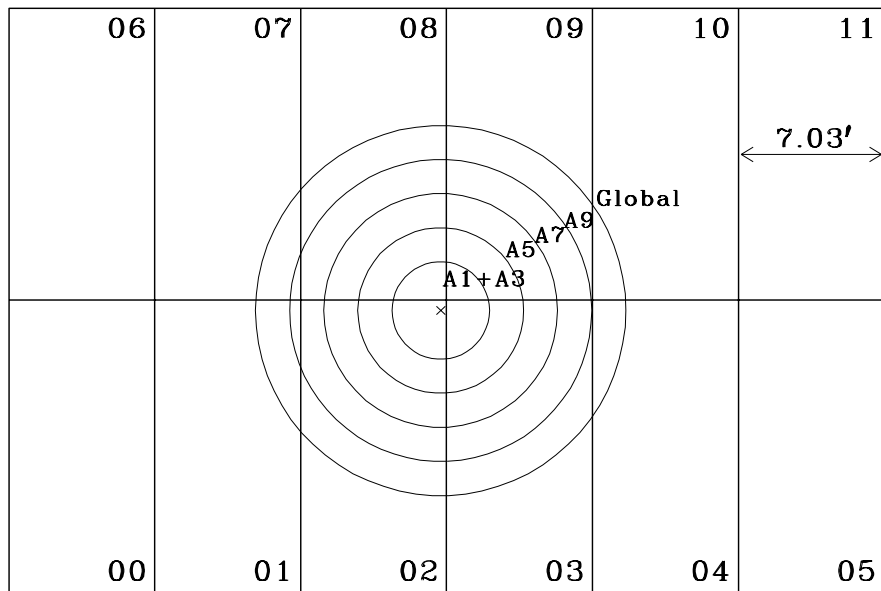


Fig. 3.— Star counts in NGC 6819. The radius of the cluster is shown to be $\sim 9.5'$. The flat distribution of stars after this point is just background. Error bars reflect both Poisson errors in the cluster and blank field star counts, and the error in locating the center of the cluster.

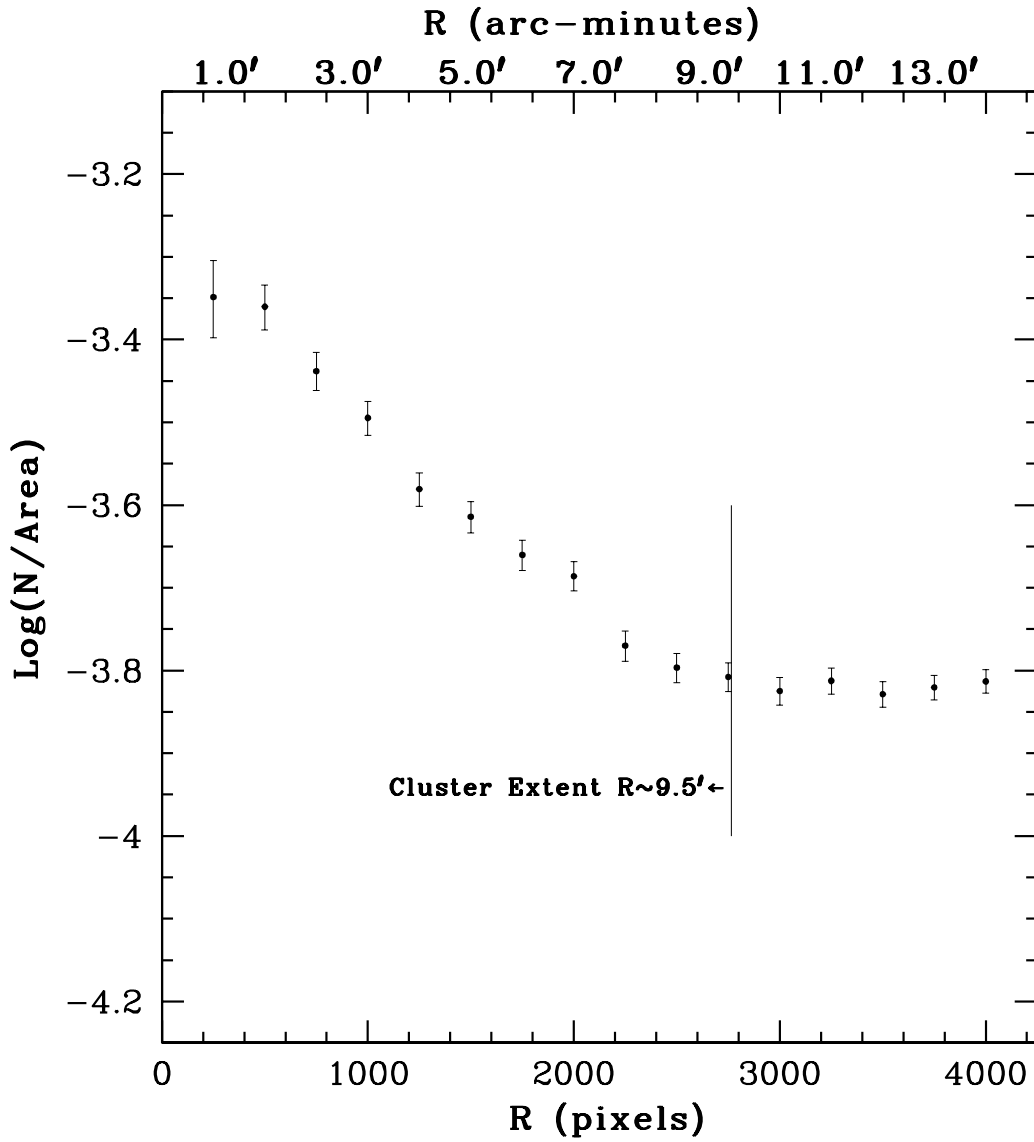


Fig. 4.— Single-mass King model shown to agree well with the cluster density distribution of NGC 6819. The arrows correspond to the core and tidal radii of the cluster. Error bars reflect both Poisson errors in the cluster and blank field star counts, and the error in locating the center of the cluster.

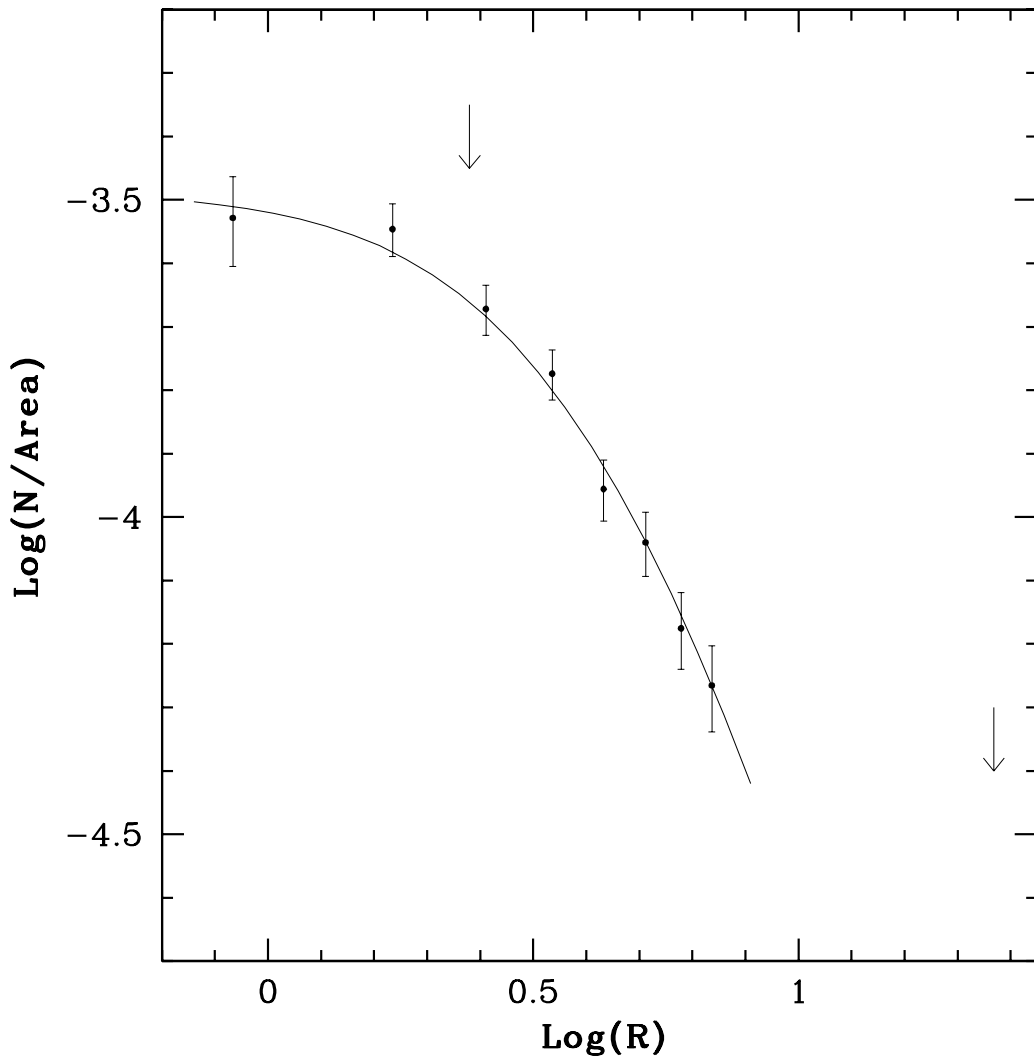


Fig. 5.— Star/galaxy classification from SExtractor indicating many sources that are most likely stellar (stellarity = 1) as well as some that are most likely galaxies (stellarity = 0). The classification of the remaining objects is addressed in §§4 and 9.2.

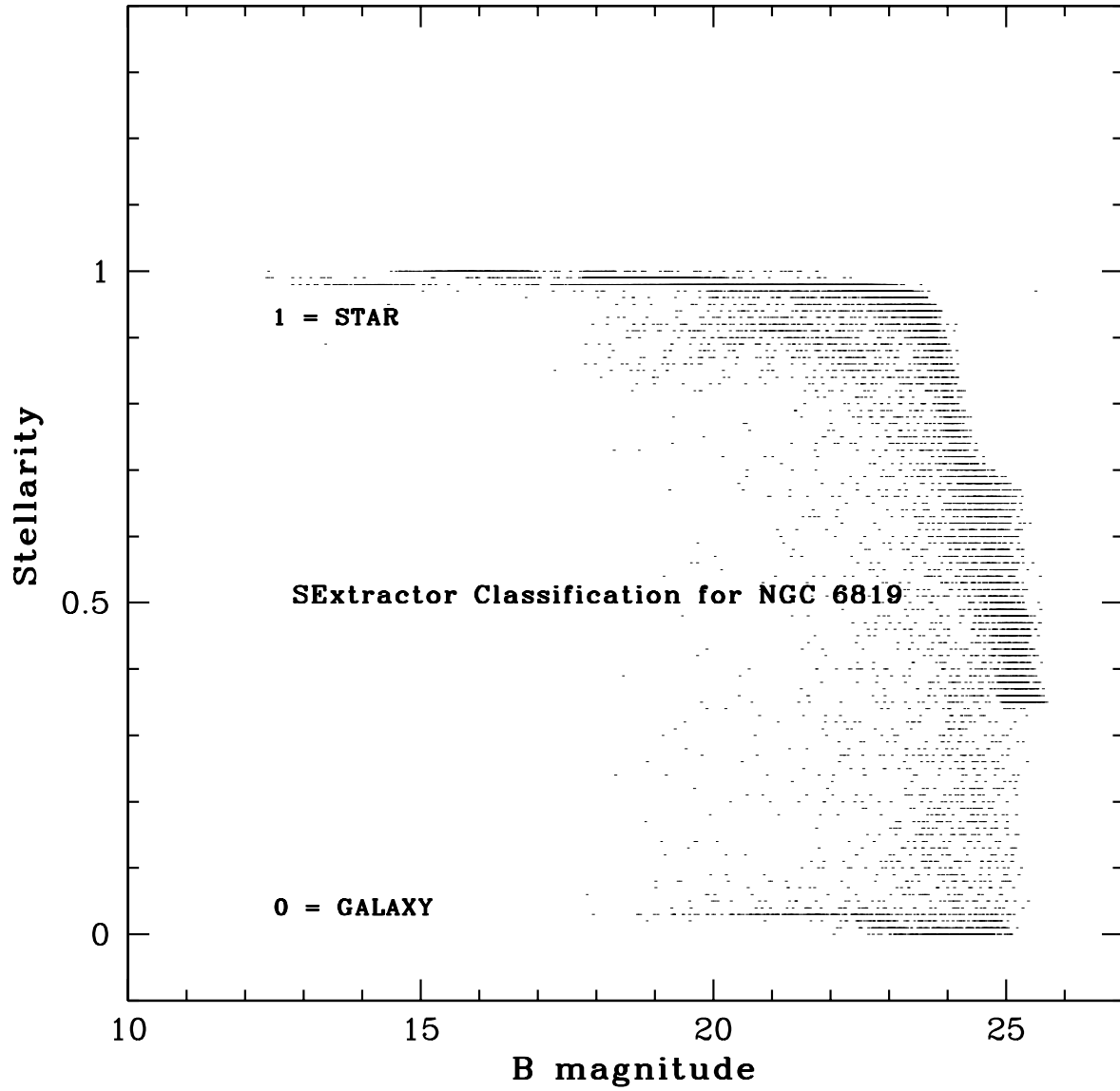


Fig. 6.— Rich, tight main-sequence and turn-off of NGC 6819, clearly seen (left). Also shown is a blank field of equal area taken from the outer four CCDs of CFH12K (right). A 0.50 stellarity cut has been applied to the data.

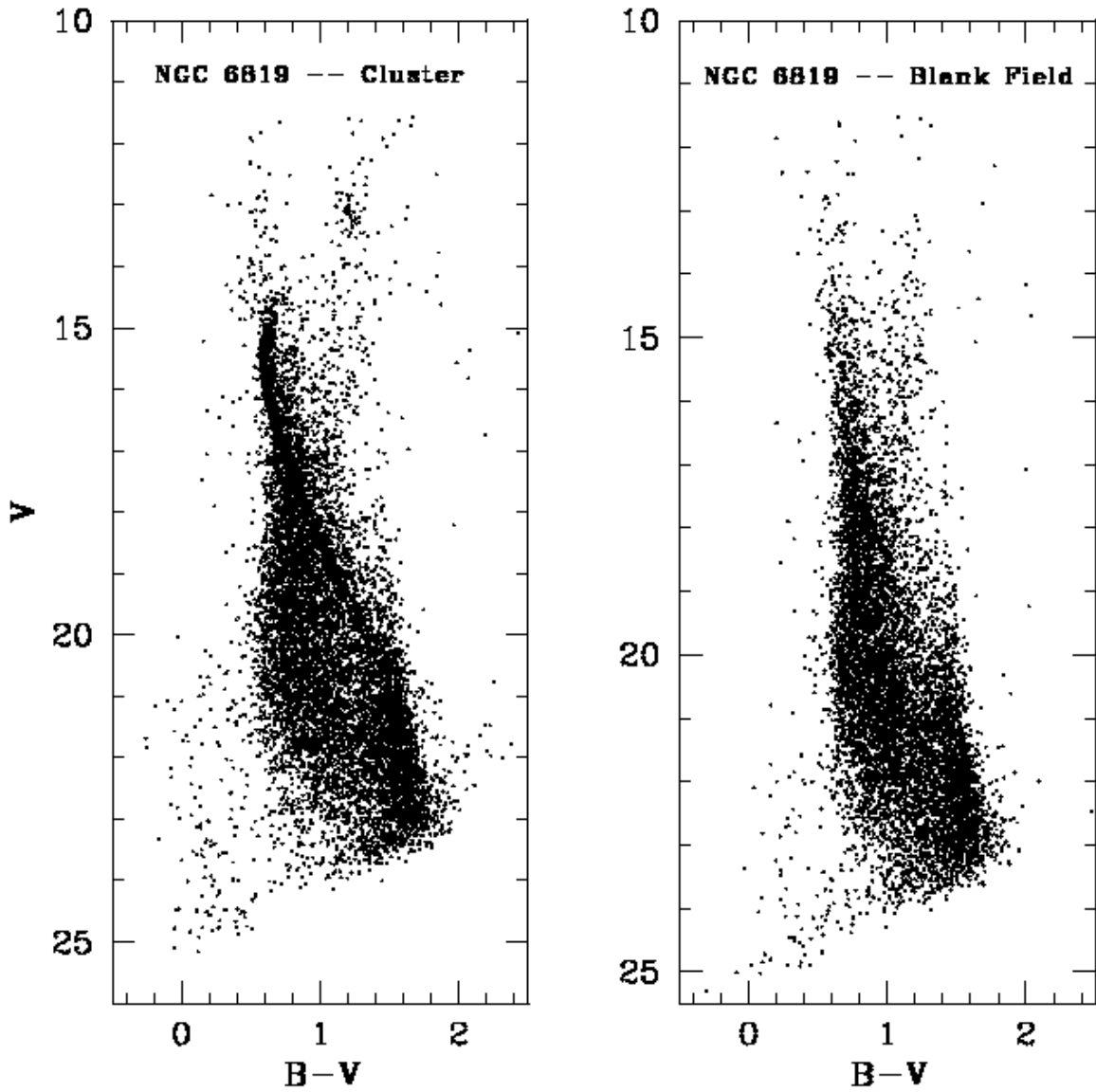


Fig. 7.— Theoretical isochrone of age 2.5 Gyr, found to fit the turn-off well. The slope of the main-sequence and the location of the red giant clump also agrees well with the isochrone. Some potential white dwarfs are also evident in the faint blue end of the CMD (we have applied a 0.50 stellarity cut).

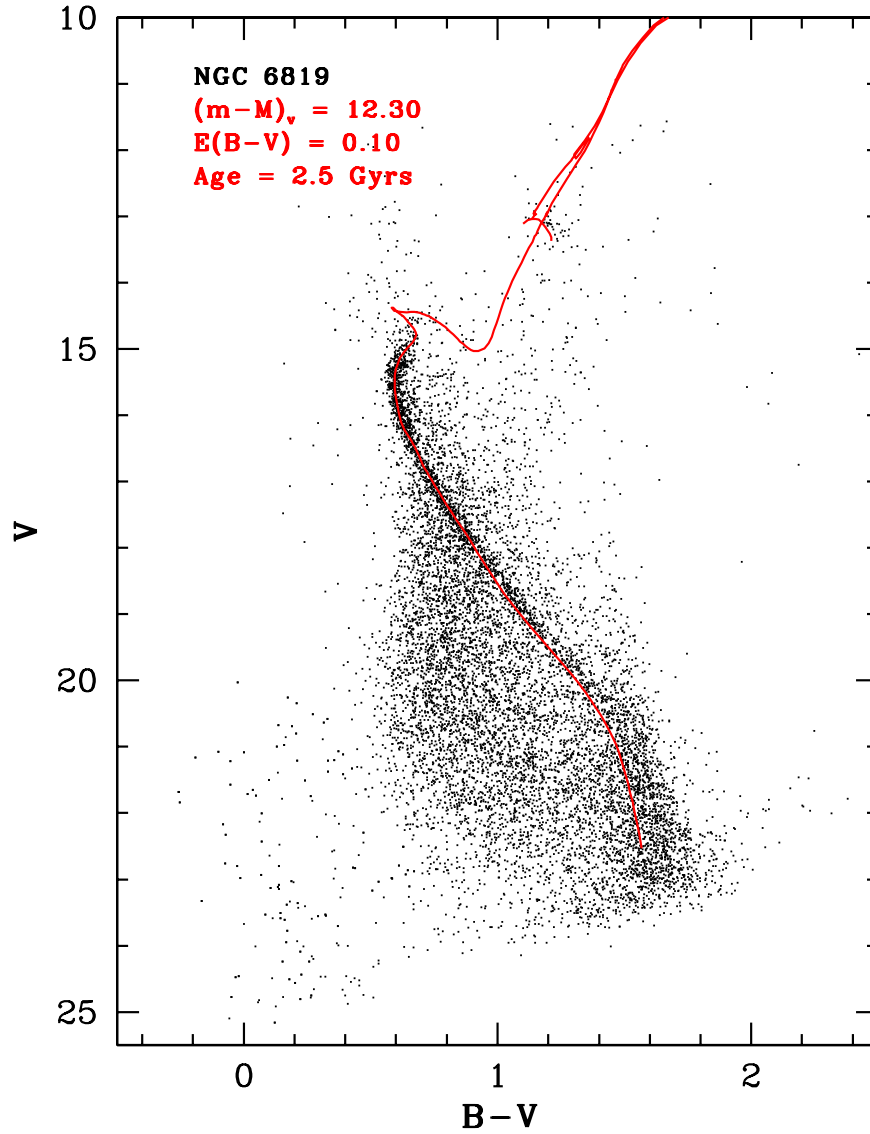


Fig. 8.— Both input stars (left) and recovered stars (right) in the incompleteness tests for both the main-sequence and potential white dwarf cooling sequence.

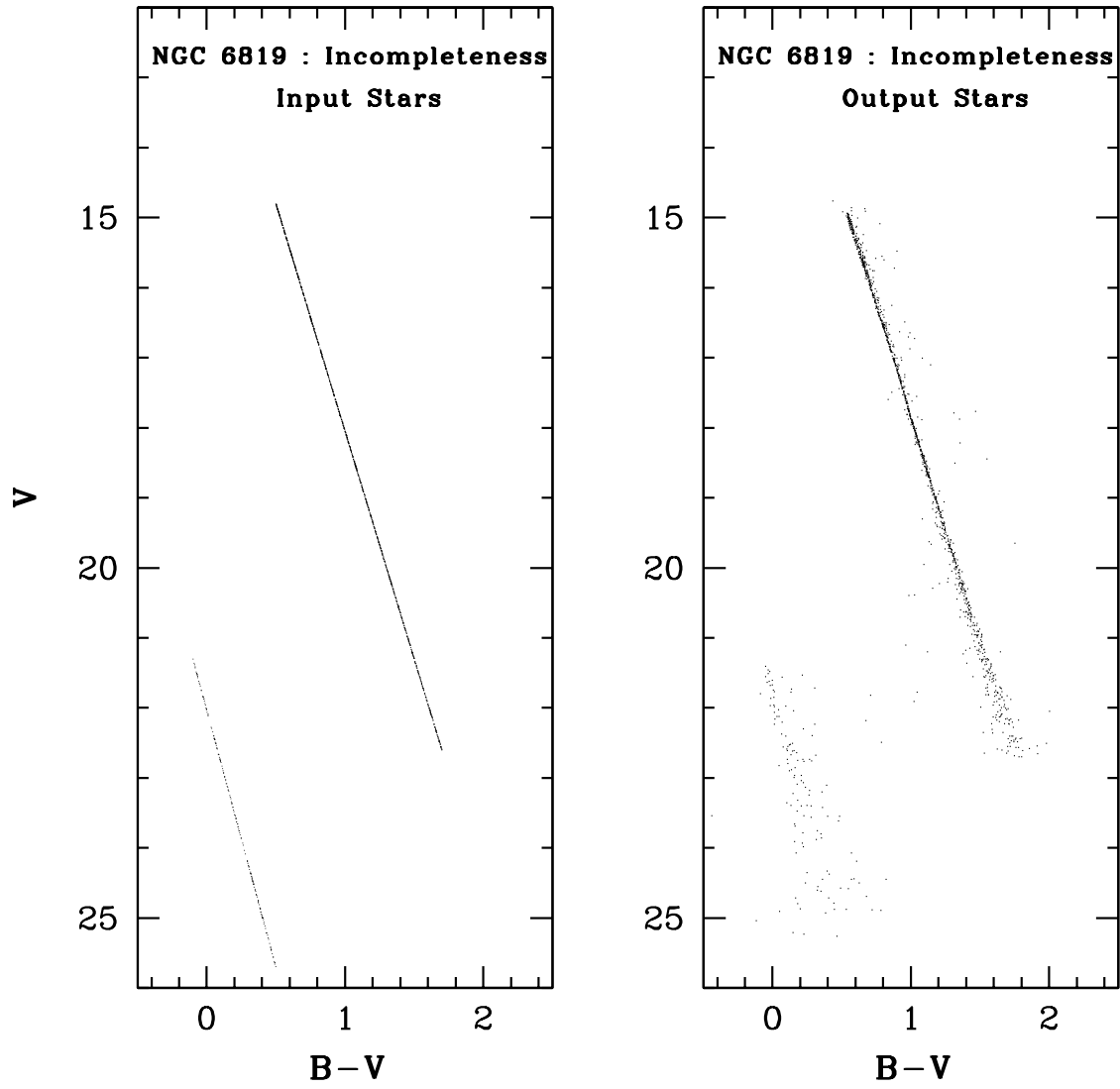


Fig. 9.— Global ($R \leq 9.5$) luminosity function shown before (dashed) and after (solid) incompleteness corrections. The almost flat luminosity function is most likely due to dynamical evolution which has caused the high mass stars to sink to the inner regions of the cluster. The error bars reflect a combination of Poisson errors and incompleteness errors as discussed in §6.1.1

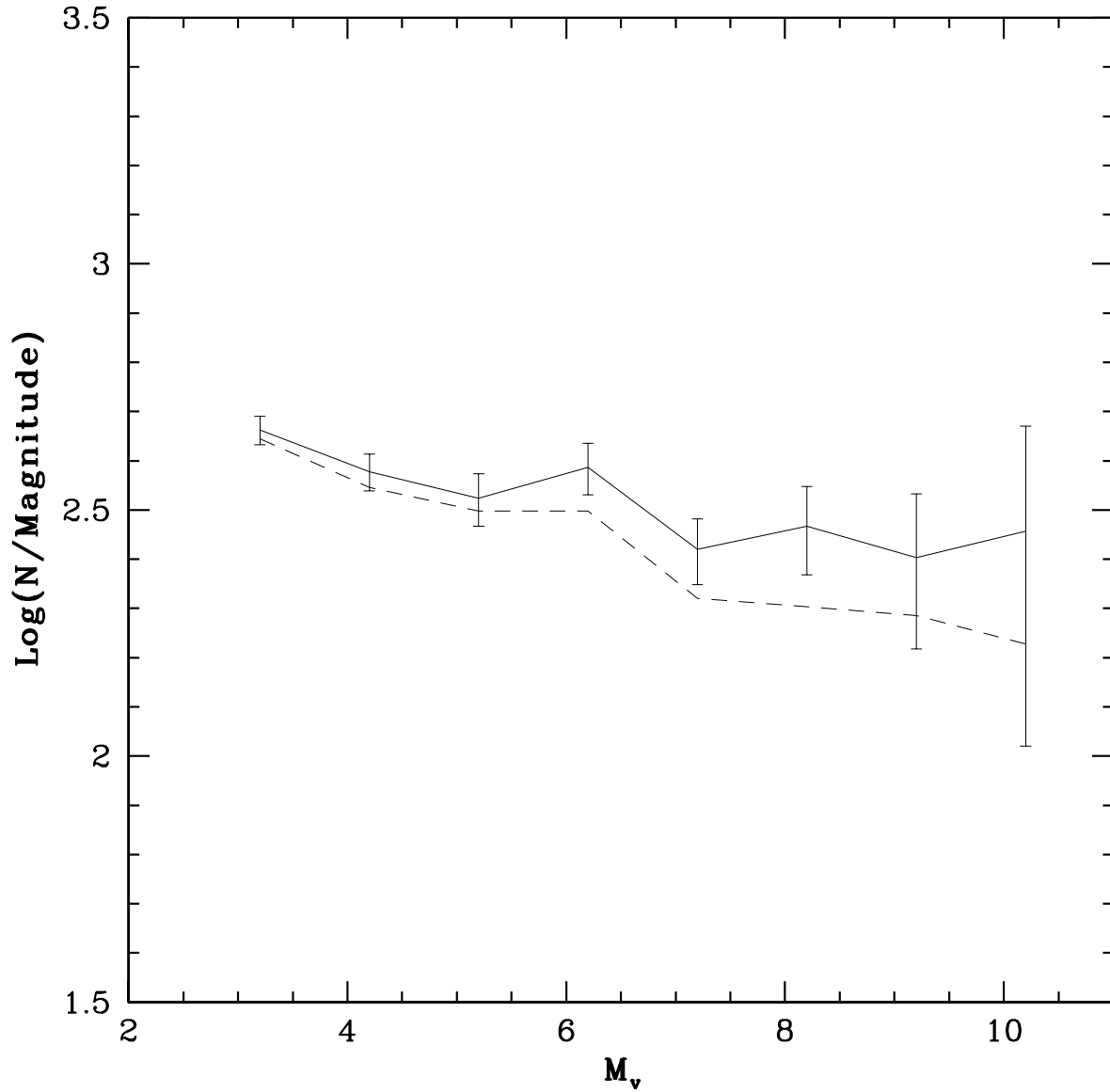


Fig. 10.— Luminosity function shown for three regions in the cluster. The counts in the central and outer annuli have been normalized to the number in the inner annulus at $V = 17$. This demonstrates clear evidence for mass segregation in NGC 6819.

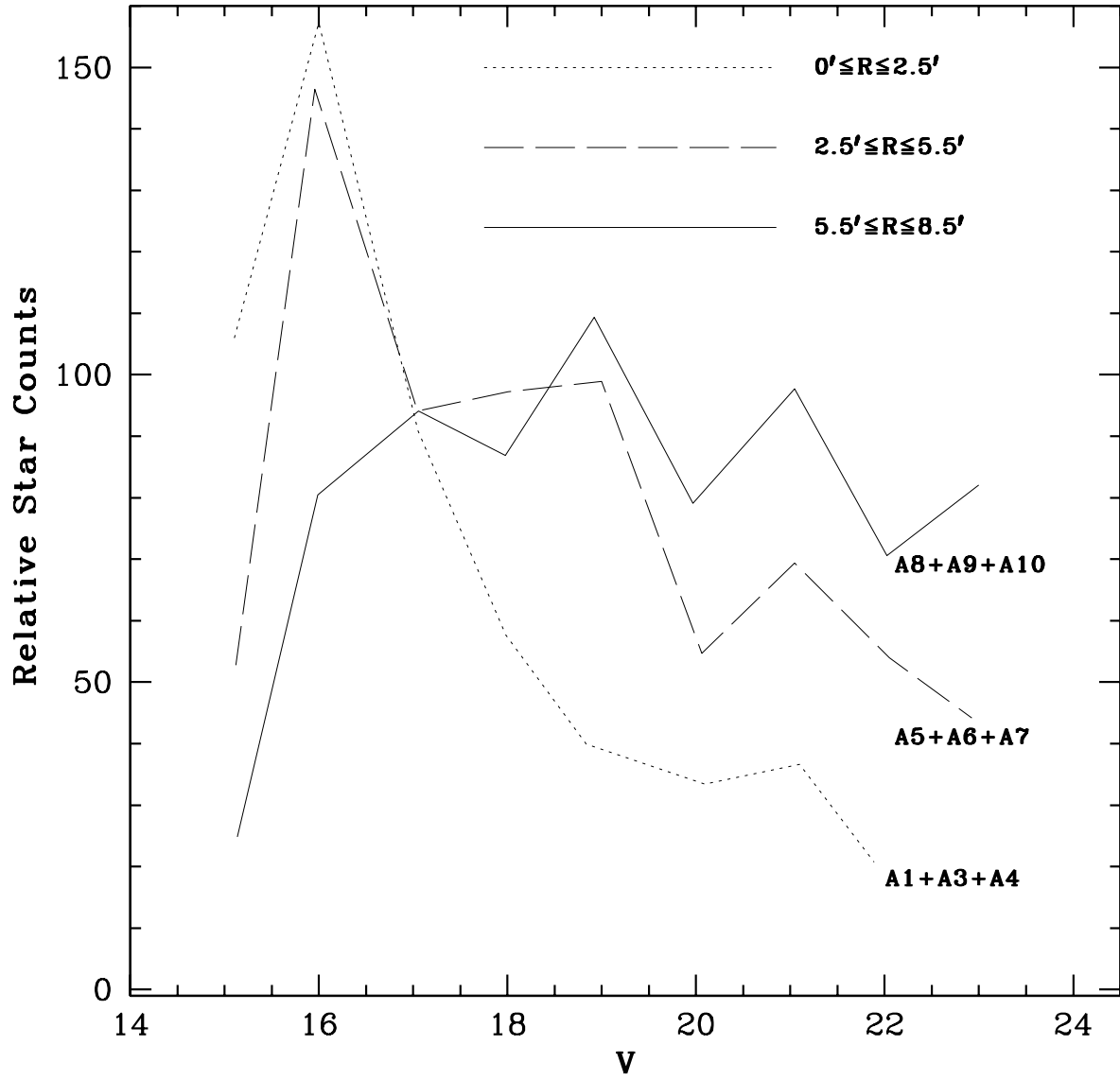


Fig. 11.— CMD for NGC 6819 for each alternate annuli, illustrating the main-sequence density as a function of increasing radius from the center. The figure shows that the lower mass (faint) stars are located in the outskirts of the cluster. A prominent binary sequence is also evident in the intermediate regions of the cluster (top right).

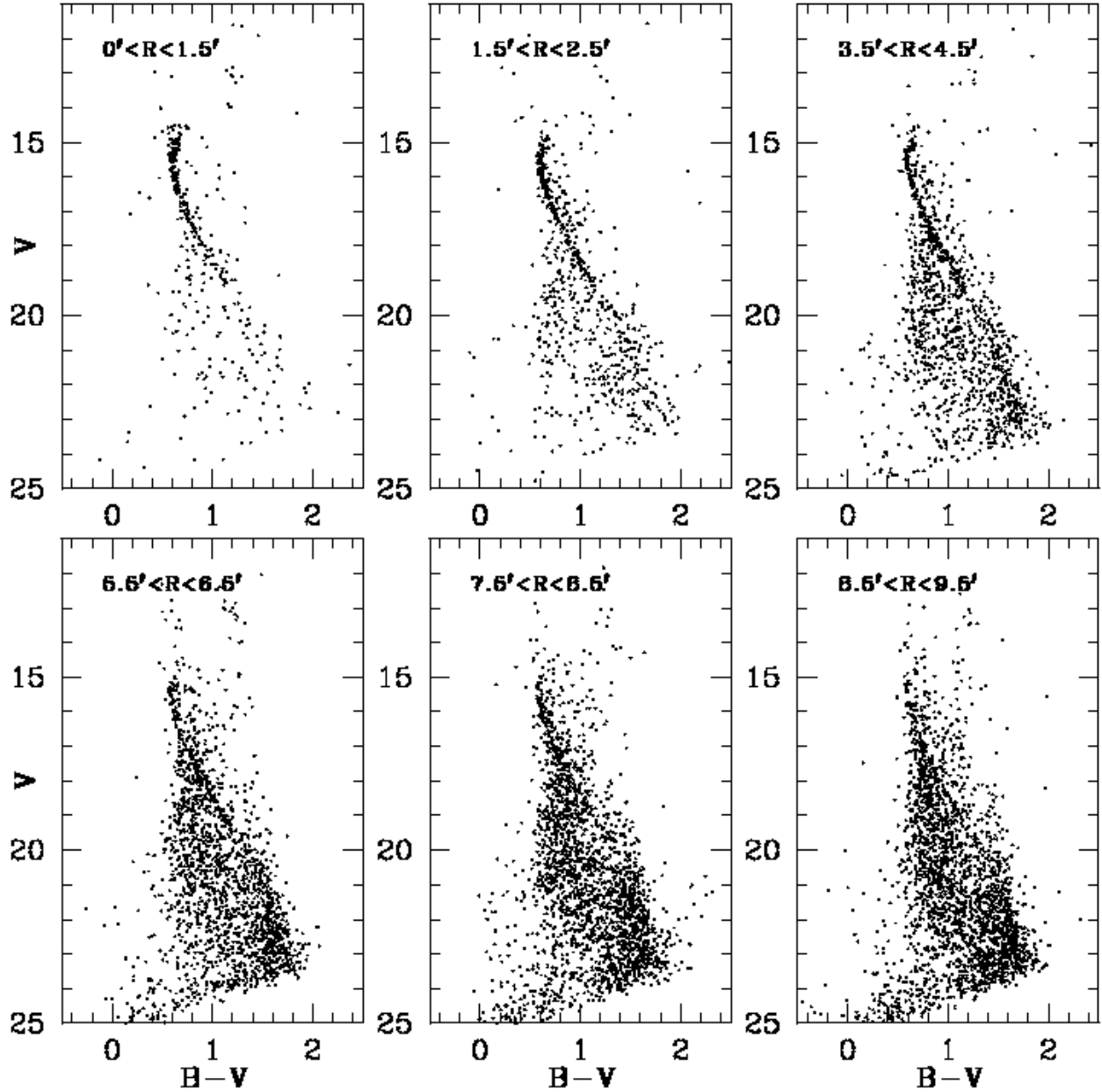


Fig. 12.— Series of mass functions for eight different annuli, illustrating a general trend of positive to negative slope as a function of increasing distance from the cluster center. The global mass function ($x = -0.15$) of the cluster is clearly flatter than a Salpeter value ($x = 1.35$, dashed line, bottom right). The error bars are taken from the errors in the luminosity functions (Poisson and incompleteness) and then multiplied by the slope of the mass-luminosity relation.

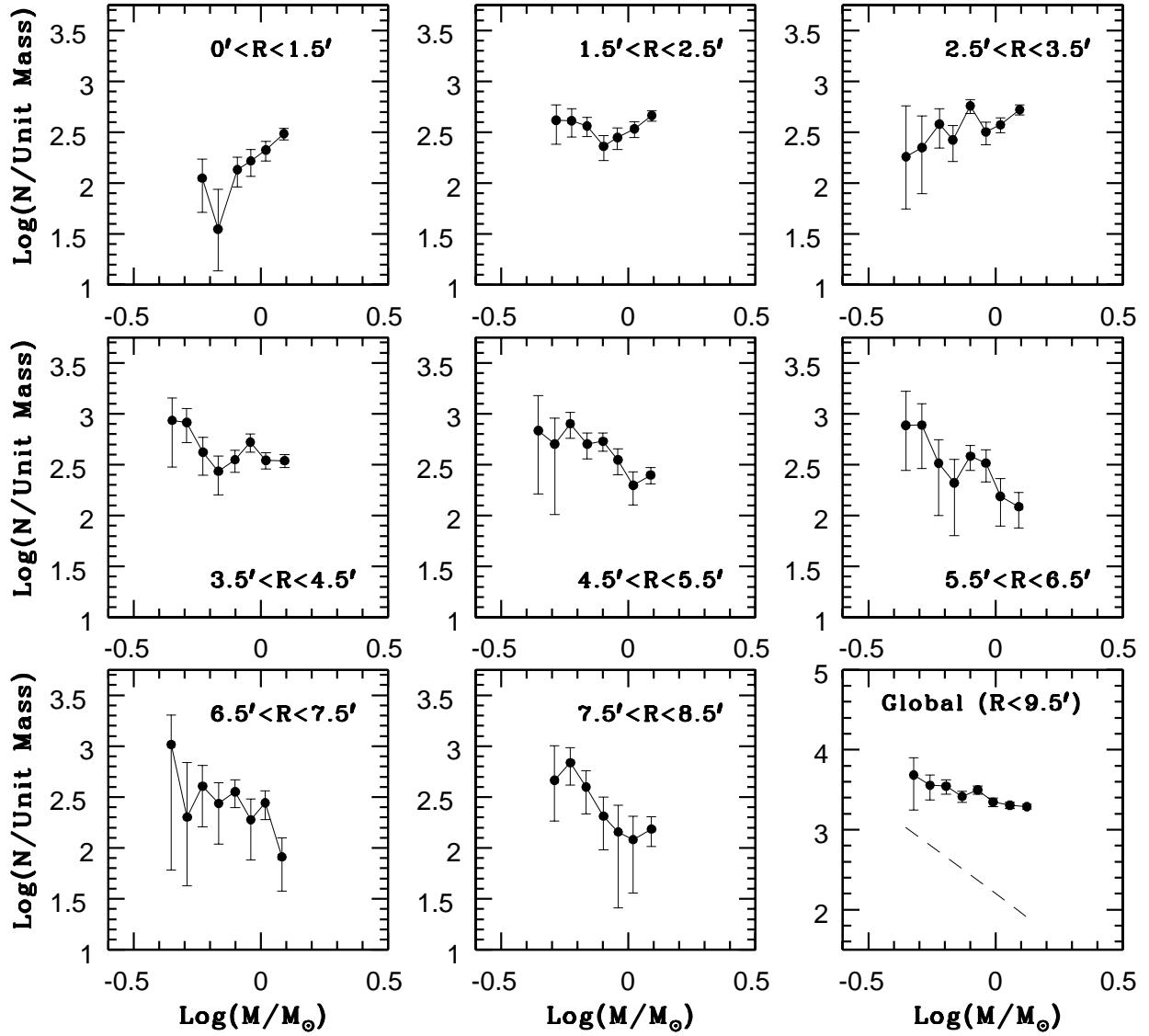


Fig. 13.— Uncorrected CMD for NGC 6819 (left). There is a general spread of stars in the lower left corner. After correcting for extended sources (center) and field star subtraction (blue of dashed line, middle), a potential white dwarf cooling sequence is evident (right). We also show a $0.7 M_{\odot}$ white dwarf cooling sequence which agrees with the bluest potential white dwarfs. This analysis is a purely statistical method of determining the most likely location on the CMD of the cluster white dwarfs.

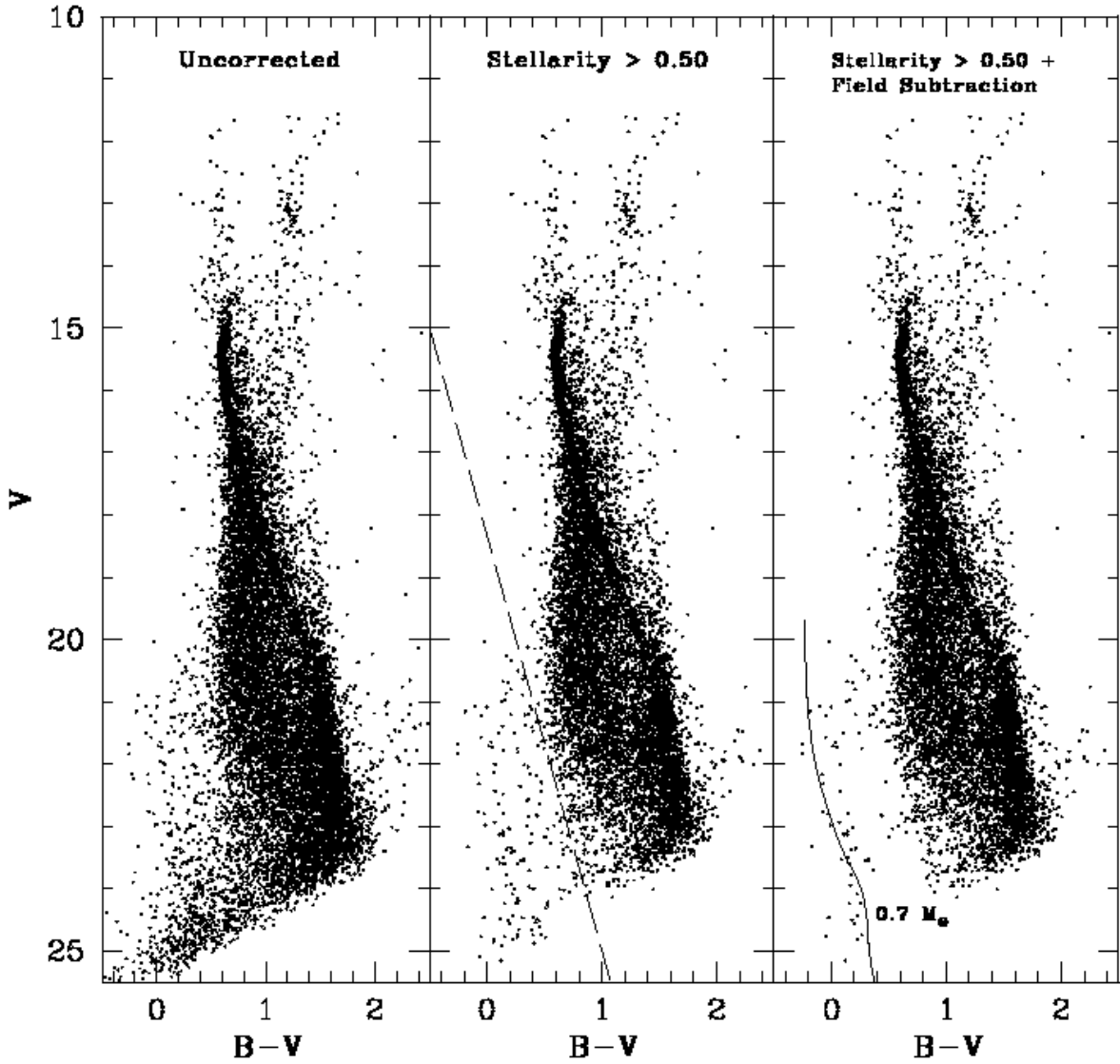


Fig. 14.— All potential white dwarf candidates within 0.3 magnitudes (color) of the $0.7 M_{\odot}$ cooling sequence and after a statistical subtraction. A photometric error bar is also shown as a function of magnitude. A large number of the objects are determined to be very high confidence stars (diamonds).

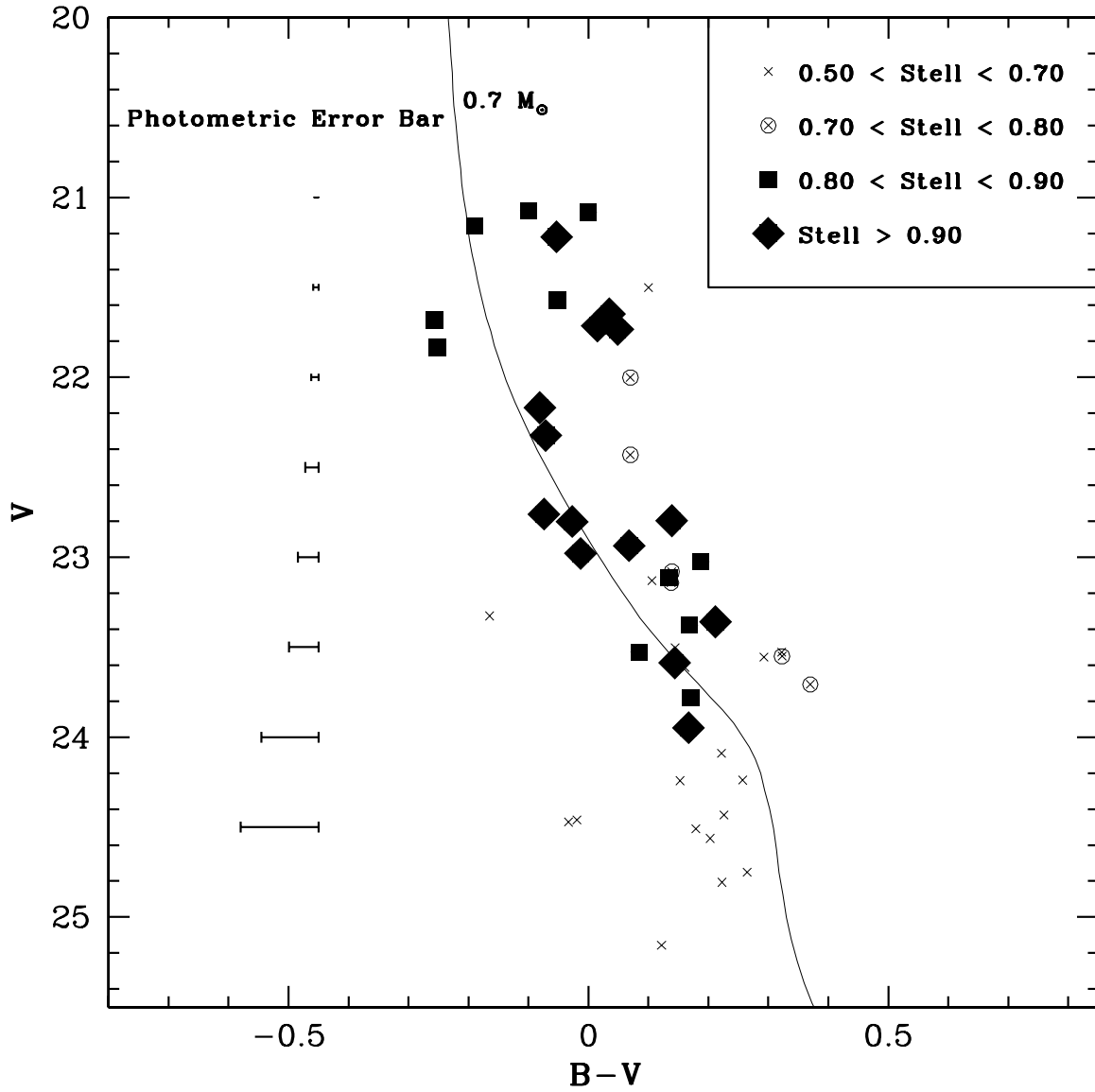


Fig. 15.— Luminosity function of the left-most trail of white dwarfs in the CMD; agrees well with the slope of the theoretical luminosity function (dashed line—see §9.3).

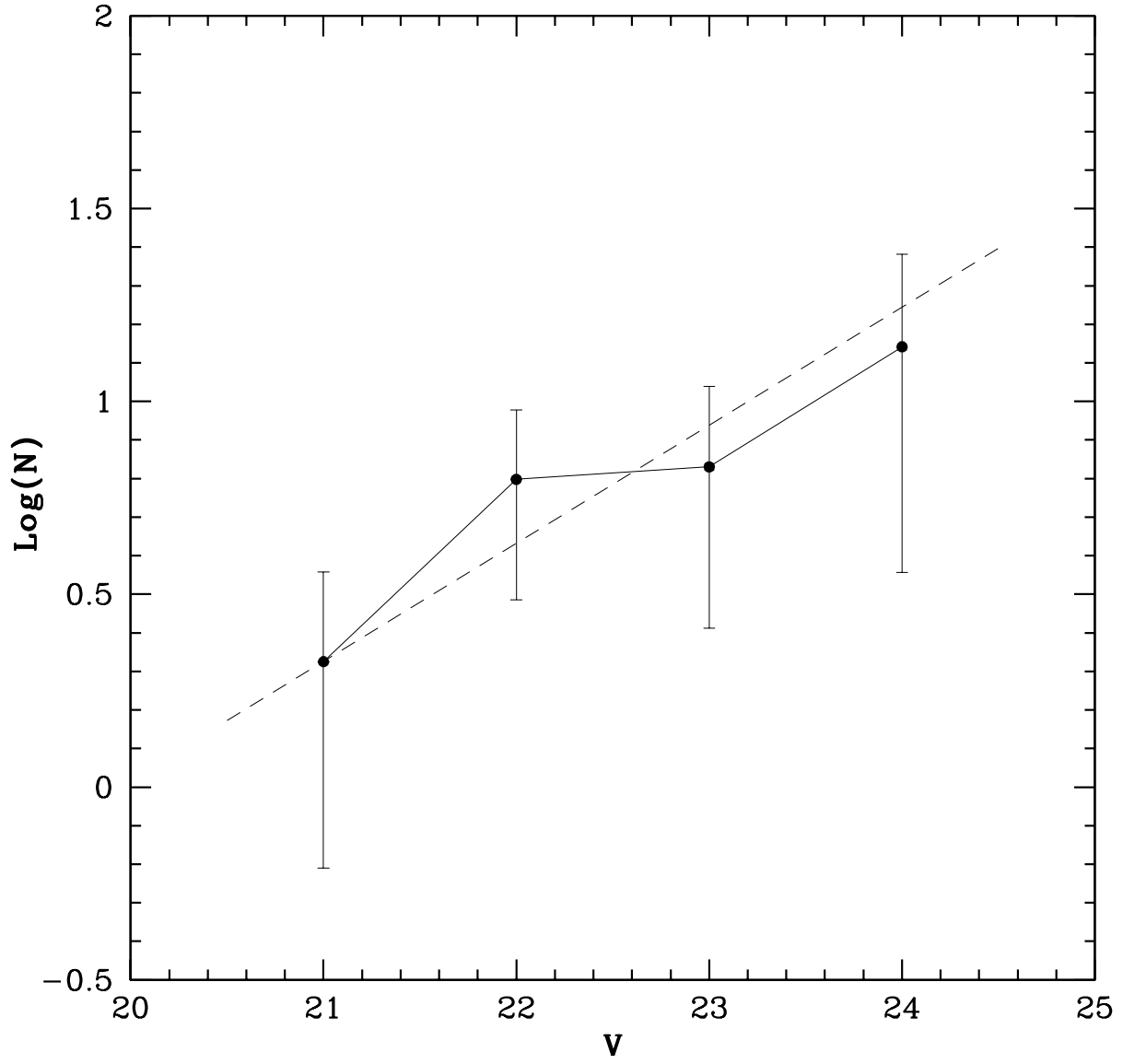


Table 1. Observational Data for NGC 6819

Filter	Exposure Time (s)	No. of Images	Seeing (")	Airmass
V	300	9	0.70	1.30
	50	1	0.70	1.16
	10	1	0.68	1.15
	1	1	0.78	1.27
B	300	9	0.90	1.40-1.76
	50	1	0.82	1.38
	10	1	0.84	1.37
	1	1	1.1	1.25
R	50	1	0.64	1.14
	10	1	0.66	1.13

Table 2. Annulus Geometry

Annulus	Radius (')	Radius (pixels)	Area (') ²
A1	$0 \leq R \leq 0.5$	$0 \leq R \leq 145$	0.51
A2	$0 \leq R \leq 1.0$	$0 \leq R \leq 291$	2.59
A3	$0.5 \leq R \leq 1.5$	$145 \leq R \leq 437$	5.74
A1+A3	$0 \leq R \leq 1.5$	$0 \leq R \leq 437$	6.25
A4	$1.5 \leq R \leq 2.5$	$437 \leq R \leq 728$	12.02
A5	$2.5 \leq R \leq 3.5$	$728 \leq R \leq 1019$	18.30
A6	$3.5 \leq R \leq 4.5$	$1019 \leq R \leq 1311$	24.58
A7	$4.5 \leq R \leq 5.5$	$1311 \leq R \leq 1602$	30.87
A8	$5.5 \leq R \leq 6.5$	$1602 \leq R \leq 1893$	37.15
A9	$6.5 \leq R \leq 7.5$	$1893 \leq R \leq 2184$	43.43
A10	$7.5 \leq R \leq 8.5$	$2184 \leq R \leq 2475$	49.72
A11	$8.5 \leq R \leq 9.5$	$2475 \leq R \leq 2767$	55.98
Global	$0 \leq R \leq 9.5$	$0 \leq R \leq 2767$	278.31

Table 3. Completeness Corrections

V mag	No. Stars Input	No. Stars Recovered (Cluster/Blank)	Completeness Correction (Cluster/Blank)
Main-Sequence			
14.5-15.0	127	122/123	1.043/1.038
15.0-15.5	126	122/124	1.035/1.016
15.5-16.0	98	93/96	1.06/1.021
16.0-16.5	107	103/107	1.047/1.000
16.5-17.0	93	84/88	1.107/1.057
17.0-17.5	90	87/88	1.038/1.023
17.5-18.0	103	92/96	1.127/1.073
18.0-18.5	96	85/91	1.133/1.055
18.5-19.0	82	76/80	1.084/1.023
19.0-19.5	84	72/76	1.176/1.105
19.5-20.0	82	70/75	1.183/1.093
20.0-20.5	71	56/60	1.283/1.183
20.5-21.0	76	58/63	1.306/1.206
21.0-21.5	62	49/50	1.28/1.248
21.5-22.0	59	42/44	1.415/1.341
22.0-22.5	44	27/31	1.664/1.419
22.5-23.0	32	19/21	1.684/1.584
23.0-23.5	20	11/12	1.818/1.667
White Dwarfs			
21.0-22.0	28	26.5/27	1.057/1.037
22.0-23.0	46	29.3/31	1.570/1.484
23.0-24.0	51	30.5/32	1.672/1.594
24.0-25.0	59	26/29	2.269/2.034

Table 4. Cluster Star Counts (Raw / Corrected)

V mag	A1+A3	A4	A5	A6	A7	A8	A9	A10	V mag	GLOBAL
15.5-16.5 (Raw)	63	91	104	68	49	23	15	29	15.0-16.0	441
Corrected	64.3 (8.4)	96.8 (11.3)	110.6 (12.1)	72.6 (10.6)	52.5 (9.4)	25.6 (9.8)	17.1 (9.3)	32.1 (10.6)		459.5 (30.4)
16.5-17.5	33	51	56	52	28	21	39	15	16.0-17.0	351
Corrected	35.4 (7.7)	57.1 (9.9)	62.7 (10.5)	58.5 (10.8)	33.2 (12.0)	25.9 (12.6)	46.4 (14.7)	20.2 (14.2)		378.5 (32.5)
17.5-18.5	20	33	37	61	40	36	19	13	17.0-18.0	315
Corrected	22.4 (6.7)	38.0 (9.1)	43.2 (10.9)	71.3 (14.6)	47.7 (13.5)	44.4 (15.5)	25.6 (15.3)	19.5 (16.0)		333.9 (40.5)
18.5-19.5	14	23	58	35	53	37	34	18	18.0-19.0	315
Corrected	15.1 (4.9)	25.5 (7.1)	63.7 (10.2)	39.2 (9.6)	59.5 (12.0)	42.5 (11.7)	39.5 (12.1)	22.8 (12.2)		385.6 (46.3)
19.5-20.5	3	28	19	19	36	12	16	25	19.0-20.0	209
Corrected	3.2 (4.7)	33.5 (7.3)	24.4 (9.3)	25.0 (10.4)	46.3 (13.3)	19.2 (13.4)	25.1 (15.1)	36.4 (16.5)		263.1 (40.3)
20.5-21.5	6	23	20	22	43	14	18	34	20.0-21.0	201
Corrected	8.6 (4.7)	31.4 (9.7)	29.1 (12.2)	32.1 (13.1)	61.3 (17.5)	25.1 (17.4)	30.9 (18.6)	52.7 (21.0)		293.4 (59.7)
21.5-22.5	0	18	8	35	18	29	2	13	21.0-22.0	193
Corrected	0	26.8 (11.2)	14.4 (10.1)	53.1 (19.3)	32.5 (25.9)	49.9 (31.3)	13.0 (10.3)	29.8 (15.4)		252.8 (87.9)
22.5-23.5	0	0	3	24	15	17	25	0	22.0-23.0	169
Corrected	0	0	10.0 (7.0)	47.1 (20.1)	37.5 (17.8)	42.0 (18.1)	56.7 (14.9)	0 (6.8)		286.6 (181.8)

Table 5. Equal Mass Binary Star Counts

Ann No.	Radius (')	No. MS Stars ($15.5 \leq V \leq 21.5$)	No. Binary Stars ($15.5 \leq V \leq 21.5$)	Percentage of Binaries (%)
A1	$0 \leq R \leq 0.5$	12 (± 6)	2 (± 1)	17 (± 12)
A2	$0 \leq R \leq 1$	71 (9)	3 (4)	4 (6)
A3	$0.5 \leq R \leq 1.5$	191 (14)	12 (6)	6 (3)
A1+A3	$0 \leq R \leq 1.5$	203 (15)	13 (6)	6 (3)
A4	$1.5 \leq R \leq 2.5$	291 (20)	34 (8)	12 (3)
A5	$2.5 \leq R \leq 3.5$	319 (21)	48 (10)	15 (3)
A6	$3.5 \leq R \leq 4.5$	287 (21)	36 (11)	13 (4)
A7	$4.5 \leq R \leq 5.5$	275 (22)	57 (13)	21 (5)
A8	$5.5 \leq R \leq 6.5$	160 (26)	6 (13)	4 (8)
A9	$6.5 \leq R \leq 7.5$	144 (26)	26 (15)	18 (11)
A10	$7.5 \leq R \leq 8.5$	110 (29)	28 (16)	25 (16)
Global	$0 \leq R \leq 9.5$	2214 (67)	242 (37.5)	11 (2)

Table 6. White Dwarf Continuity Analysis – Predicted Number vs. Observed Number

V mag cut	Observed (Raw)	Observed (Corr)	Pred (0.6 M_{\odot})	Pred (0.7 M_{\odot})	Pred (0.8 M_{\odot})
For 0.80 Stellarity Cut					
13.0 \pm 3.6 Red Giants					
$t_{RG} = 9 \times 10^7$					
≤ 24	27 (± 5)	53 (± 7)	61 (± 17)	55 (± 16)	48 (± 14)
≤ 23.5	21 (5)	35 (6)	29 (8)	25 (7)	21 (6)
≤ 23	17 (4)	28 (6)	11 (3)	9 (3)	8 (2)
For $t_{RG} = 7 \times 10^7$					
≤ 24	27 (5)	53 (7)	78 (22)	71 (20)	61 (17)
≤ 23.5	21 (5)	35 (6)	37 (10)	32 (9)	27 (8)
≤ 23	17 (4)	28 (6)	15 (4)	12 (3)	10 (3)
For $t_{RG} = 5 \times 10^7$					
≤ 24	27 (5)	53 (7)	109 (31)	99 (28)	86 (24)
≤ 23.5	21 (5)	35 (6)	52 (15)	44 (13)	38 (11)
≤ 23	17 (4)	28 (6)	20 (6)	17 (5)	14 (4)
For 0.90 Stellarity Cut					
$t_{RG} = 9 \times 10^7$					
≤ 24	17 (4)	34 (6)	61 (17)	55 (16)	48 (14)
≤ 23.5	13 (4)	22 (5)	29 (8)	25 (7)	21 (6)
≤ 23	12 (3)	19 (5)	11 (3)	9 (3)	8 (2)
For $t_{RG} = 7 \times 10^7$					
≤ 24	17 (4)	34 (6)	78 (22)	71 (20)	61 (17)
≤ 23.5	13 (4)	22 (5)	37 (10)	32 (9)	27 (8)
≤ 23	12 (3)	19 (5)	15 (4)	12 (3)	10 (3)
For $t_{RG} = 5 \times 10^7$					
≤ 24	17 (4)	34 (6)	109 (31)	99 (28)	86 (24)
≤ 23.5	13 (4)	22 (5)	52 (15)	44 (13)	38 (11)
≤ 23	12 (3)	19 (5)	20 (6)	17 (5)	14 (4)